

**Design and Implementation of an
XUV-pump IR-probe Transient Grating
Experiment**

Tadas Balčiūnas
Lund Reports on Atomic Physics, LRAP-408
Lund, June 2009

Summary

In this work a transient grating pump-probe measurement technique and its application to study the evolution of secondary electron cascades in diamond crystal is presented. The particular type of pump-probe experiment described in this thesis allows studying matter interaction with high energy photons. After absorption of the high energy photon, an energetic electron can create more electron-hole pairs in the sample through impact ionization thus dissipating the initial kinetic energy and resulting in a so-called electron cascade. In other words, an electron or a hole with high enough kinetic energy can knock a bound electron from a valence band into conduction band.

In our experiment a coherent radiation in extreme ultraviolet spectral range obtained via high harmonic generation in a noble gas is used to excite the diamond crystal sample which is subsequently probed with an infrared light pulse. A sample is excited by superimposing two coherent extreme ultraviolet pump beams at an angle. The absorbed extreme ultraviolet photons excite electrons to the conduction band that lead to the periodic refractive index change of the transparent diamond crystal. In other words, a transient phase grating is imprinted in the sample.

The main advantage of the transient grating method is that the signal is inherently background free which leads to a high sensitivity of the measurement. The short duration of the extreme ultraviolet pulse and the possibility to synchronize high harmonic and optical pulses with unprecedented precision make it possible to achieve temporal resolution of the order of several tens of femtoseconds which is required to study extremely fast dynamics in matter. Time resolution required for electron cascade measurements is on the order of tens of femtoseconds which is not available in case of synchrotron or free electron laser radiation.

The two high harmonic beams are generated by splitting the infrared beam into two separate beams in a Michelson interferometer and focusing them into a gas cell at a slightly different angle. Because of the inherent low conversion efficiency of the high harmonic generation (of the order of 10^{-5}), the two extreme ultraviolet pump beams traveling at a small angle are then focused using a high numerical aperture reflective objective in order to achieve sufficient energy density on the sample. In order to achieve high contrast of the interference pattern a multilayer narrow band coating of the objective mirrors is used to filter the bandwidth of the generated high harmonic spectrum.

In this thesis the principle of the transient grating measurement technique as well as detailed feasibility and optimization calculations of the optical setup parameters are presented. The experimental setup is implemented to a large degree and the initial experimental tests are described.

Sammanfattning

Detta arbete är en del i förberedelsen inför en kommande studie av andra ordningens elektronkaskader i diamant. Den grundläggande idén bakom mättekniken förklaras och en design av den experimentella uppställningen presenteras där ett transient gitter spelar en central roll. En teoretisk optimering av signalen från det transienta gittret är utförd och beräkningar visar att den effektiva diffraktionen är tillräcklig för det kommande experimentet. Interferens är sedermera verifierad experimentellt från två XUV strålar. En ny och viktig detalj i uppställningen är ett multilagerobjektiv som samtidigt filtrerar och focuserar XUV strålen. Det nya objektivet leder till bättre upplösning i tiden eftersom man nu kan undvika att filtrera signalen i efterhand med ett diffraktionsgitter.

Contents

1	Introduction	6
1.1	Motivation	6
1.2	Outline	7
1.3	High harmonic generation	7
1.4	Secondary electron cascades	15
2	Method	16
2.1	The transient grating measurement technique	16
2.2	Optimization of experimental setup parameters	18
2.3	Optical setup	25
3	Experimental setup	35
3.1	The Terawatt laser system	35
3.2	The flat field spectrometer	39
3.3	Nonlinear effects in optical elements	42
4	Results	43
4.1	The measurement of HHG spectrum	43
4.2	Far-field measurements	45
4.3	Interference fringe pattern measurement	47
5	Conclusion and outlook	50
5.1	Acknowledgements	50
A	Schwarzschild objective parameters	50
B	Focal length of the two-lens optical system	52

1 Introduction

1.1 Motivation

The development of ultrafast lasers during the last two decades [1] has opened up new realms of science. Pulses on the order of femtosecond (10^{-15} s) have made it possible to track chemical reactions in time and opened a completely new field of science: femtochemistry. Furthermore, recent achievements in attosecond science have led to research on even faster events, such as the motion of an electron [2].

Unlike femtochemistry pump-probe experiments where visible or infrared optical pulses are used, our aim is to implement a particular type of pump-probe experiment that allows to study matter interaction with high energy photons that can excite inner shell electrons. The problem was suggested by Jan Isberg and his collaborators from Division for Electricity at Uppsala University. The research in a field of diamond electronics has promising applications in industry and basic science [3]. A robust theory of diamond interaction with high energy photons has been developed [4], and there is a great demand for the actual dynamics measurements with high temporal resolution.

To achieve this goal an original concept based on induced transient grating using two high harmonic XUV beams interference is presented. We use high harmonic generation [5] to generate coherent radiation in extreme ultraviolet (XUV) spectral range to excite sample which is subsequently probed with an infrared light pulse. A phase grating is imprinted in the sample by superimposing two coherent XUV pump beams at an angle. Absorbed XUV radiation excites electrons into conduction band that lead to refractive index change of the transparent material. A delayed infrared probe pulse diffracts due to periodicity of induced refractive index change in the sample and is detected using a detector. Because it is a background-free measurement, it makes possible to measure small changes in the refractive index.

The temporal resolution is one of the most important aspects of the proposed technique. The ability to synchronize high harmonic XUV and optical pulses with unprecedented precision makes it possible to study extremely fast dynamics in matter. Pulses obtained via high harmonic generation are unique because of their short duration (≈ 10 fs) and coherence [6]. Time resolution required for electron cascade measurements is on the order of tens of femtoseconds which is not available in case of synchrotron or free electron laser radiation. Note that our experiment is essentially different than ultra-fast X-ray diffraction pump-probe experiments [7] where a strong optical pump pulse is used to excite matter and a weak X-ray pulse is used to probe the dynamics. In our experiment the XUV pulses are used to excite the matter and optical pulses are used to probe the refractive index change.

In this thesis is a principle of transient grating measurement technique as well as detailed feasibility and optimization calculations of optical setup parameters are presented. The experimental setup is implemented to a large degree and the initial experimental tests are performed.

1.2 Outline

The first chapter provides an introduction to the physics of the high harmonic generation process and the secondary electron cascades. The transient grating measurement technique together with estimations of experimental setup parameters are presented in the second chapter. In the third chapter the technical aspects of the experiment are presented along with the optical scheme of XUV spectrometer, a short description of the terawatt laser system and the techniques used for its alignment. The fourth chapter describes the main measurement results. As the main result of this report an interference fringe pattern of two XUV beams is presented. Finally the report is concluded in the last chapter. Additionally the description of the Schwarzschild objective and a calculation of the effective focal length of a two lens optical system using paraxial geometrical optics is described in the appendix.

1.3 High harmonic generation

The subject of nonlinear optics has been rapidly evolving since the first demonstration of second harmonic generation [8] shortly after the laser was invented. In the beginning the research, was mainly focused on low-order nonlinear processes. For relatively low laser field intensities, the nonlinear response of material is described using a Taylor expansion of the polarization induced in the medium in the power series of the electric field strength:

$$P(t) = \chi^{(1)}E(t) + \chi^{(2)}E(t)^2 + \chi^{(3)}E(t)^3 + \dots \quad (1)$$

Such a regime is called perturbative nonlinear optics regime. With the development of pulsed lasers and increasing peak powers the studies of atoms in strong laser fields became possible. If the strength of the electric field becomes comparable to the Coulomb potential of the atom, the above expansion is not valid anymore. Strong field physics gained substantial attention when above-threshold ionization (ATI) was discovered [9]. It was discovered that energy spectrum of electrons produced by photo-ionization consisted of multiple peaks spaced by the laser photon energy $\hbar\omega_0$.

In 1987 an efficient photon emission in the extreme ultraviolet (XUV) range was observed for the first time [10]. These observations suggested that atoms exposed to strong laser fields can emit coherent high-harmonic radiation at photon energies much higher than the atomic ionization potential. Odd harmonics $q\omega_0$ of the driving laser field ω_0 are generated up to some certain cut-off q_{max} [11]. The peculiar property is that most high harmonics are generated with similar efficiency which is a characteristic property of a non-perturbative process. To the contrary, the low-order harmonics are converted less efficiently with increasing order.

One of the first observations of high-harmonic generation demonstrated spectra up to 33rd harmonic generation in Ar, Kr and Xe gases [10]. Intensities of the order of 10^{13} W/cm² were used. The achievable photon energies in the first

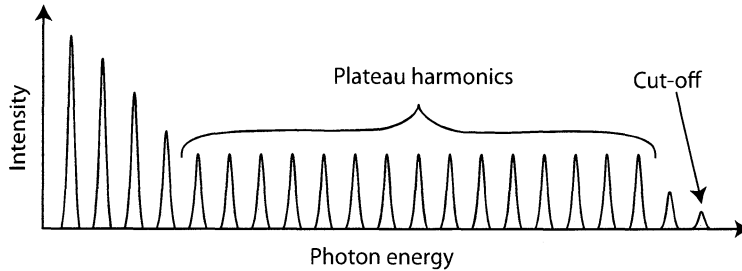


Figure 1: Typical structure of high harmonic generation spectra.

experiments were limited by long laser pulses that were used to generate harmonics. With relatively long laser pulses (100 fs - 1 ps) all the atoms interacting with the laser are ionized on the rising edge of the pulse, without being exposed to the peak intensity. Later using shorter pulses and larger intensities (of the order of 10^{15} W/cm²) allowed observing harmonics as high as 135th in Ne. Using ultra-short few optical cycle driving pulses photon energies up to 700 eV were generated [12]. Such photon energy corresponds to $\lambda = 1.77$ nm wavelength and $\approx 450^{\text{th}}$ harmonic.

1.3.1 Ionization

High harmonic generation is inextricably associated with photo-ionization. Three main mechanisms of photo-ionization that take place at different intensities are depicted in Figure 2. For relatively low intensities the main mechanism is multiphoton ionization. The Keldysh parameter (also known as the adiabaticity parameter) is often used to determine the dominant regime of photo-ionization:

$$\gamma = \sqrt{\frac{I_p}{2U_p}} \quad (2)$$

In this expression I_p and U_p are ionization and ponderomotive potentials respectively. The adiabaticity parameter can also be regarded as the ratio of the laser frequency ω_0 to the tunneling frequency $\omega_t = q_e E_0 / \sqrt{2m_e I_p}$ of an electron, that is $\gamma = \omega_0 / \omega_t$. Here q_e , E_0 and m_e are the charge of an electron, the amplitude of the laser electric field and the mass of an electron. Multiphoton ionization takes place when $\gamma > 1$ and it can be often described within perturbation theory. However, once a sufficiently high intensity is reached ($\gamma < 1$), tunnel ionization becomes the dominant mechanism. The electron tunnels directly through the quasi-stationary potential barrier which is superposition of the atomic Coulomb field and the laser field. As the intensity increases even more, over-the-barrier ionization occurs. Extremely intense femtosecond laser pulses can reach intensities much beyond 10^{15} W/cm². In that case the electric field is strong enough to suppress the atomic potential barrier and electrons can simply move into the continuum freely.

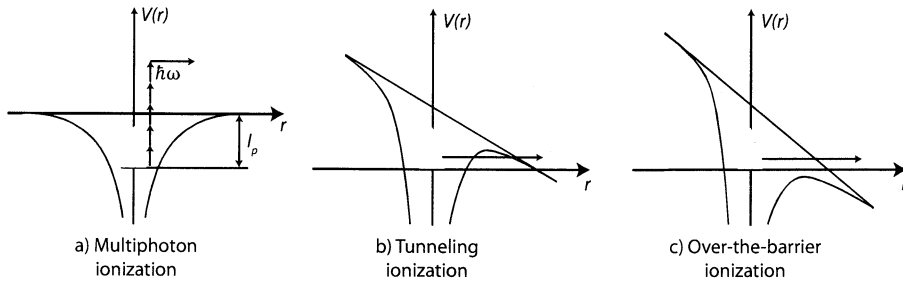


Figure 2: Three types of ionization that occur at different intensity levels.

1.3.2 Semi-classical three step model

High harmonic generation can be qualitatively explained using semi-classical three step model proposed by Corkum [13]. The three steps are depicted in Figure 3. An atom is exposed to a strong linearly polarized laser field. First, an electron from the outer shell tunnels through the barrier of the atomic Coulomb potential perturbed by the strong laser field. The quasi-free electron then follows the electrical field oscillations and subsequently acquires kinetic energy from it. The mean kinetic energy of the electron accelerated in the electric field of strength E is called ponderomotive potential:

$$U_p = \frac{q_e^2 E^2}{4m_e \omega_0^2} \quad (3)$$

Here $\omega_0 = 2\pi c/\lambda_0$ is the angular frequency of the driving laser field, q_e and m_e are the charge and mass of the electron respectively. It is convenient to express the ponderomotive potential with an expression $U_p = 9.33 \times 10^{-14} I \lambda_0^2$ [eV], where I is the intensity in W/cm^2 units and λ_0 is wavelength in μm . The electron returns to the ground state of the parent ion approximately half of an optical cycle later. Half of the electrons are ionized at the positive maximum and the other half ionized at the negative maximum of the electric field. In the vicinity of the parent ion, the electron recombines to the ground state with a small probability and emits a photon with the kinetic energy gained in the laser field and the ionization energy of the atom. As the recombination occurs twice during the optical period, the emitted XUV radiation spectrum consists of the odd harmonics spaced by twice the laser frequency. In other words, the emitted radiation is periodic and the period with a period equal to 1.3 fs for 800 nm driving laser field. The maximum harmonic number is expressed in terms of ionization potential I_p and kinetic energy that the electron gains in electric field U_p and corresponds to the cut-off in the harmonic spectrum [11]:

$$\hbar\omega_0 q_{max} = 3.17U_p + I_p \quad (4)$$

The ponderomotive potential is mainly determined by the maximum laser intensity that the neutral atoms can be exposed to before they are depleted

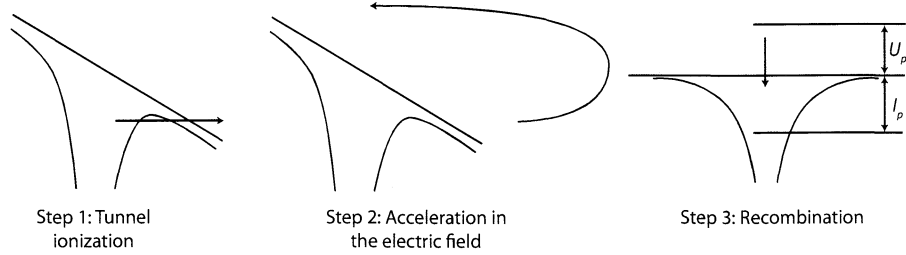


Figure 3: Illustration of the three step model of high-harmonic generation.

by ionization. This intensity increases with decreasing laser pulse duration. Therefore, in order to achieve reasonable conversion efficiency, it is desirable to have as short a laser pump pulse as possible [14]. The highest photon energies were generated using few-cycle laser pulses [12].

The electric field strength is related to intensity as follows:

$$I = \frac{1}{2} \epsilon_0 c |E|^2 \quad (5)$$

For example for a near infrared laser with $\lambda_0 = 800 \text{ nm}$ and $I = 2 \times 10^{14} \text{ W/cm}^2$, the maximum kinetic energy is $3.17U_p = 38 \text{ eV}$. The ionization potential of Argon is 15.8 eV . So, it leads to the maximum photon energy 54 eV ($\lambda = 23 \text{ nm}$, cut-off harmonic order 35).

The evolution of the electron trajectory in the oscillatory laser field can be described using simple Newtonian mechanics. It is assumed that after the ionization the electron is exposed to a time-dependent electric field $E(t) = E_0 \sin(\omega t)$ and the resulting force is expressed as:

$$F(t) = -q_e E(t) = -q_e E_0 \sin(\omega t) \quad (6)$$

The electron position can be obtained from (6) by integrating it two times:

$$x(t) = \frac{q_e E_0}{m\omega^2} [\sin(\omega t) - \sin(\omega t_i) - \omega(t - t_i) \cos(\omega t_i)] \quad (7)$$

The initial position is assumed to be zero at $t = t_i$ where t_i is the tunnel ionization time. The electron motion in the electric field is depicted in Figure 4.

The amount of energy the electron gains in the electric field as a function of tunneling time is shown in Figure 5. There are two possible electron trajectories that result in the same return energy (except for the maximum energy). The trajectory that corresponds to longer excursion time is called long trajectory, whereas that with the shorter excursion time is referred to as short trajectory. These two trajectories merge at the peak (cut-off) energy.

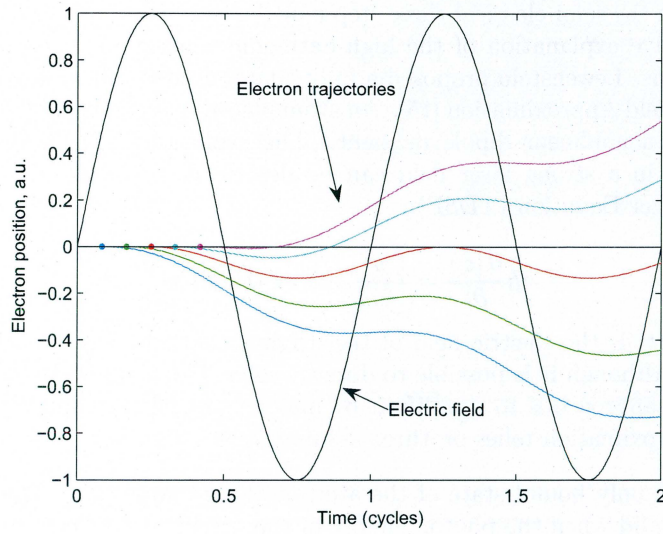


Figure 4: Classical electron trajectories in the electric external field calculated using (7) for different tunneling times t_i . Only the paths of the electrons that were born in the first half cycle are shown.

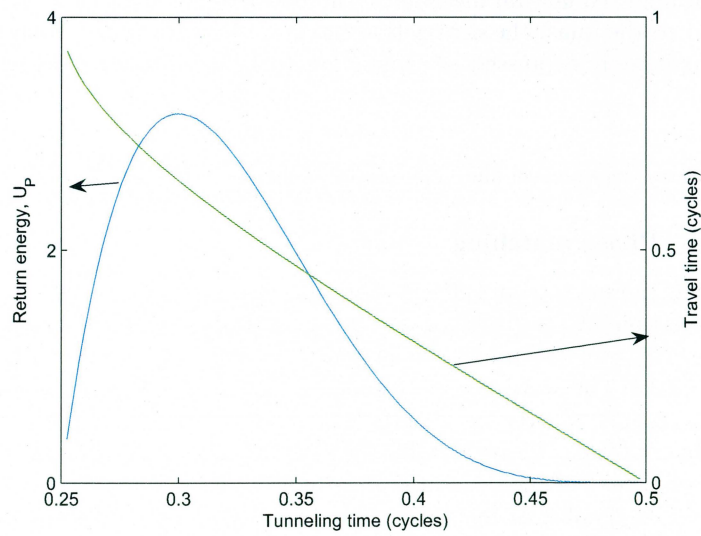


Figure 5: Electron return energy and excursion time as a function of ionization time.

1.3.3 Strong Field Approximation

Although the semi-classical three step model described in Section 1.3.2 provides an intuitive explanation of the high-harmonic generation, it has some serious limitations. Lewenstein proposed a fully quantum mechanical model based on a Strong Field Approximation [15]. An atom placed in an external electromagnetic field has a nonlinear dipole moment. The evolution of the wave function of an atom in a strong laser field can be described using the Time Dependent Schrödinger Equation (TDSE):

$$i\hbar \frac{\partial |\psi\rangle}{\partial t} = \left[\frac{p^2}{2m} - q_e r E(t) + V(r) \right] |\psi\rangle \quad (8)$$

where $E(t)$ is the electric field of the driving field and $V(r)$ is the atomic potential. Although it is possible to directly solve TDSE numerically [16], a more practical approach is to simplify it by making several assumptions. The strong field approximation relies on three assumptions:

- The only bound state of the atom is the ground state. This assumption is valid when the photon energy of the driving laser field is much smaller than ionization potential: $I_p \gg \hbar\omega_0$.
- The electron after tunneling is not affected by the atomic Coulomb potential and can be considered as a free particle in the continuum. For this assumption to be true, the laser field must be strong. This condition can be expressed using the ponderomotive potential: $I_p < 2U_p$.

According to quantum mechanics, the phase of the emitted radiation is proportional to the quasi-classical action integral. However, the atomic phase can be approximately expressed as proportional to the intensity I of the laser field:

$$\varphi_{atomic} = \alpha_q I \quad (9)$$

where α_q depends on the type of trajectory and on the harmonic order.

1.3.4 Phase matching

Besides the microscopic effects, high harmonic generation is highly affected by propagation effects. In the gas cell the field of the specific harmonic builds up coherently over the coherence length $L_c \approx \pi/\Delta k$, where Δk is the wave vector mismatch. The wave vector mismatch is proportional to the phase difference $\Delta\varphi$ accumulated over the length L of the medium. In general it depends on a number of terms. Phase matching greatly affects the amplitude of the generated harmonic field. If the generation is properly phase-matched, the harmonic yield scales with number of generating ions as N^2 . An overview of the phase matching problem is presented in this chapter because of the importance of high harmonic efficiency and pulse energy in our experiment.

As shown in Fig 5, electrons have different excursion times that depend on the instant of time for ionization. They can also return in two different

trajectories. The phase accumulated by the electron while it moves in free space is transferred to the emitted wave after it recombines. Therefore the phase of the emitted harmonic radiation is not only dependent on the phase of driving laser field but also has an intrinsic phase which varies rapidly with laser intensity.

A simple modeling of phase matching can be achieved using a one dimensional approximation model [17] that takes into account the phase mismatch of the harmonic and the driving infrared field and the absorption of XUV radiation in the generating medium. The phase mismatch can be expressed as a sum of four terms:

$$\Delta k_q = \Delta k_q^g + \Delta k_q^p + \Delta k_q^d + \Delta k_q^f \quad (10)$$

The first term Δk_q^g is the phase mismatch due to dispersion in the neutral gas. If n_q is the refractive index of q^{th} harmonic we have:

$$\Delta k_q^g = (n_q - n_1) \frac{q\omega_0}{c} \quad (11)$$

The second term Δk_q^p is the phase mismatch due to the generated plasma. This term is always present as high harmonic generation is inextricably related to ionization. Similarly to the dispersion term Δk_q^g , the plasma term also depends on the difference of the refractive index due to free electron: $n_q^p = \sqrt{1 - \omega_p^2/(q\omega)^2}$. The $\omega_p = \sqrt{N_e q_e^2/(m_e \epsilon_0)}$ is the plasma frequency. The wave-vector mismatch can be expressed as:

$$\Delta k_q^p = (n_q^p - n_1^p) \frac{q\omega_0}{c} \quad (12)$$

The third term in (10) is the phase mismatch due to the change of the dipole phase which is caused by the variation of the intensity along the beam in the gas cell:

$$\Delta k_q^d = \frac{\partial}{\partial z} \left(\frac{\alpha_q I_0}{1 + (z/z_R)^2} \right) \quad (13)$$

where $z_R = 2\pi w_0^2/\lambda_0$ is the Rayleigh range. The last term Δk_q^f takes into account effects due to focusing of the fundamental Gaussian beam. In general, the amplitude of the Gaussian beam is given by:

$$E(r, z) = E_0 \frac{w_0}{w(z)} \exp\left(-\frac{r^2}{w(z)^2}\right) \exp[-i\varphi(r, z)] \quad (14)$$

where the phase factor is:

$$\varphi(r, z) = kz + \frac{kr^2}{2R(z)} - \zeta(z) \quad (15)$$

The first term is simply the phase of the plane wave characterized by the wave number $k = \omega_0/c$. The second term is a curvature of the wavefront. The

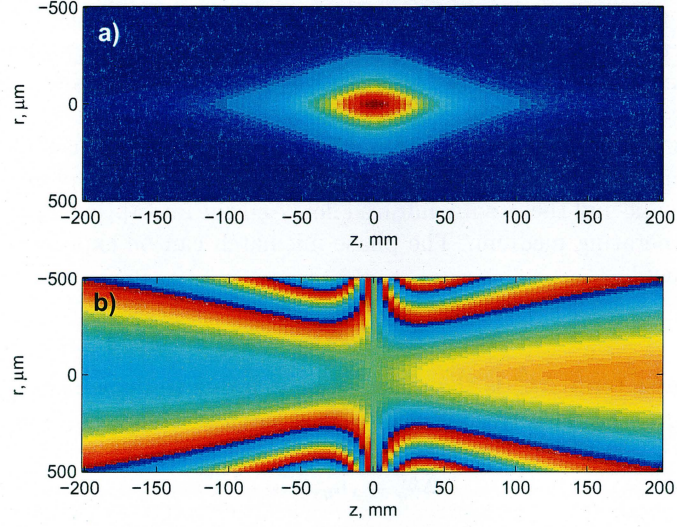


Figure 6: Distribution of (a) intensity and (b) phase of the IR pump beam.

radius of curvature $R(z) = z \left[1 + (z_R/z)^2 \right]$ is expressed in terms of the Rayleigh range. The third term represents the Gouy phase: $\zeta(z) = \tan^{-1}(z/z_R)$ which affects the phase matching and should be included into the calculation. So, the last term in (10) in general can be expressed as:

$$\Delta k_q^f = (q-1) \frac{\partial}{\partial z} \left(\tan^{-1} \frac{z}{z_R} \right) \quad (16)$$

Moreover, the Gouy phase also has an effect on the carrier envelope phase [18]. However, this effect can be neglected in our experiment, because relatively long pulses (that consist of many optical cycles) are used and no carrier envelope phase stabilization is performed. In our experiment the pump beam is focused into the gas cell using a spherical mirror of $f_p = 2$ m focal length. The beam is usually clamped using an iris, approximating it as a Gaussian beam of radius d_{in} (diameter of the iris) the waist radius of the pump beam is equal to:

$$w_0 = \frac{2\lambda_0 f_p}{\pi d_{in}} \quad (17)$$

For illustration the intensity and phase distribution of the pump beam is shown in Figure 6 for a typical beam diameter value $d_{in} = 15$ mm.

Besides the phase mismatch between the harmonic and driving infrared beam, the emitted harmonic radiation is absorbed in the generating medium by a $\exp(-\kappa_q L/2)$. The absorption coefficient κ_q is usually expressed in terms of an absorption cross-section σ_{ph} and neutral atom density ρ_{at} :

$$\kappa_q = \sigma_{photo} \rho_{at} \quad (18)$$

For practical purposes it is desirable to maximize the intensity of some particular harmonic. In the strong absorption limit and in a one-dimensional approximation this is true when

$$F_q = \frac{1}{\sqrt{\Delta k_q^2 + \kappa_q^2}} \quad (19)$$

is maximized.

Quasi-phase-matching can also be employed to enhance the efficiency of high harmonic generation. A rather simple way to achieve quasi-phase-matching is to use a hollow core waveguide filled by neutral gas [19, 20]. This technique allows increasing the harmonic yield by two orders of magnitude in some conditions. The modulated diameter hollow core fibers allow to enhance the generation process even further and to achieve higher photon energies. It was demonstrated that filamentation of ultra-short pulses may also help to achieve phase-matching [21]. However, the above mentioned quasi-phase-matching techniques are efficient in case of low pump pulse energy. In our setup loose focusing geometry and high pump pulse energies were used to achieve large (up to 10^{10}) photon number per harmonic per pulse.

1.4 Secondary electron cascades

A material irradiated by X-ray photons emits energetic photoelectrons. This effect is known as photoelectric effect and is widely used in metrology to characterize materials. Following the emission of an energetic photoelectron from an inner shell, the emission of an Auger electron takes place as illustrated in Figure 7 (a) and (b). These electrons then create electron-hole pairs in the sample through impact ionization thus dissipating the initial kinetic energy and resulting in a so-called electron cascade.

The Auger effect is a transition of an electron in an atom to an inner-shell vacancy and the emission of another electron due to the released energy. The high energy photon can remove the electron from a core orbital of an atom. An electron from a higher energy level can move to a lower energy state and release the energy either in the form of photon or transfer it to another electron with smaller binding energy which is subsequently ejected. The term Auger electron is usually used to denote the ejected electron. The kinetic energy of the Auger electron is equal to the difference between the transition energy to the core orbital and the ionization of the electron from the shell from which the Auger electron was emitted.

Similar to the atomic case discussed above, Auger recombination also takes place in crystals and condensed media. The difference is that as electron-hole pair recombines, the energy is transferred to another electron in the conduction band. Auger recombination is a three-body process and scales with the cubic

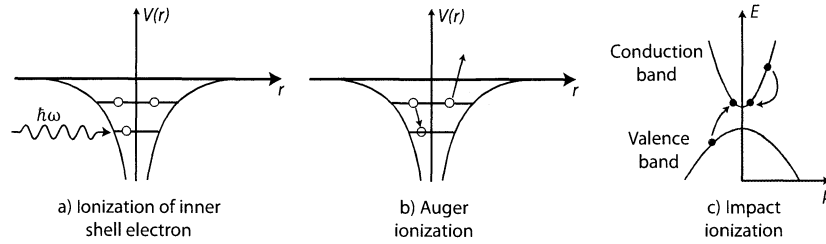


Figure 7: An illustration of the Auger ionization process. (a) An inner shell electron of an atom is photoionized by a high energy photon, thereby creating a short-lived inner shell vacancy. (b) The outer shell electron fills in vacancy and the energy is transferred to the other outer shell electron that is subsequently ejected from the atom. (c) An illustration of the impact ionization process in a bulk material.

power of the carrier concentration. The impact ionization is the reverse process to the Auger recombination. The electron or hole with a high kinetic energy can lose its energy and create one electron-hole pair as shown in Figure 7 (c). In other words, an electron with enough kinetic energy can knock a bound electron from a valence band into conduction band. The impact ionization is the main mechanism of the electron cascades.

A Monte Carlo model was derived by Ziaja et al. that describes the evolution of electron cascades induced by photo-electrons in diamond [4]. Although the theory of electron cascades is rather mature, there are very few actual measurements. The electron-hole pair creation energy after the exposure to ultrashort hard x-ray pulses was recently measured [22]. Even though femtosecond XUV pulses were used to excite the electron cascades, there were no measurements of electron cascade dynamics. The experiment described in this work should allow us to measure the early evolution of an electron cascade and give valuable information about the underlying process. The process occurs very rapidly on a time scale of 0.1-100 fs.

2 Method

2.1 The transient grating measurement technique

In this work a transient grating pump-probe measurement technique and its application to study the evolution of secondary electron cascades is presented. The main advantage of the transient grating method is that the signal is inherently background free which leads to a high sensitivity of the measurement. The short duration of the harmonic XUV pulse and the possibility of sending pump and probe pulses nearly collinearly make it possible to achieve temporal resolution of the order of several tens of femtoseconds. A basic scheme of the experiment is shown in Figure 8. Two coherent XUV pump beams are super-

imposed on the sample at an angle and interference fringes are formed. Due to periodic refractive modulation induced by the interference pattern, a phase grating is formed. Absorbed pump radiation produces free electrons that lead to refractive index change (see Section 2.2.2 for estimations). Subsequently, a delayed infrared probe pulse diffracts through an induced grating in the sample and is detected using a photo diode.

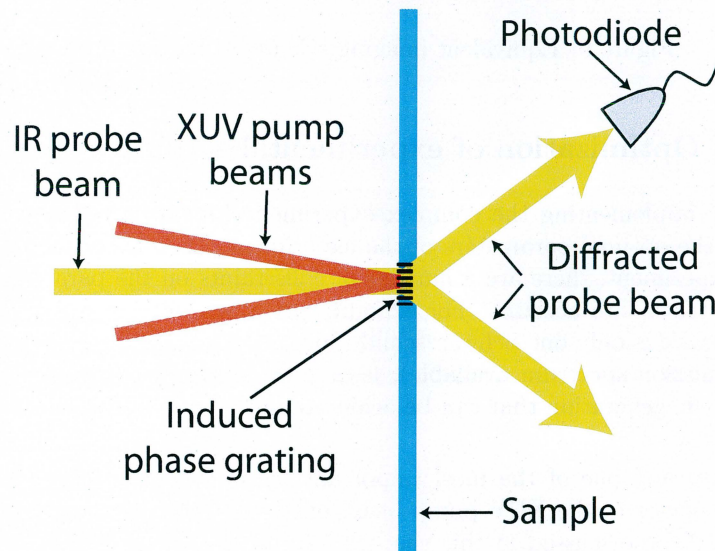


Figure 8: Basic scheme of the temporal electron cascade evolution measurement using the induced grating technique.

Two major ways were employed to produce interference HHG radiation patterns. The first way is essentially a Young double slit experiment: a single XUV beam is generated and afterwards two pinholes are used to produce two coherent point sources. Such method was initially used to demonstrate spatial coherence of the high harmonic beam [23]. This scheme was also used for wave-front phase measurements of XUV radiation [24]. However, the drawback of such an approach is that most of the XUV pulse photons are lost. A much more efficient and clever way to generate two high harmonic beams is to split the infrared beam into two separate beams in a Michelson interferometer and to focus them into a gas cell at a slightly different angle [25]. Such an approach was demonstrated for XUV interferometric measurements [26, 5] and was chosen in our experiment. The two XUV pump beams traveling at an angle β are then focused using a high numerical aperture Schwarzschild objective in order to achieve sufficient energy density. The Schwarzschild objective can be represented as a thin lens as shown in Figure 9. The sample is placed after the focal plane of the objective where the two beams overlapped.

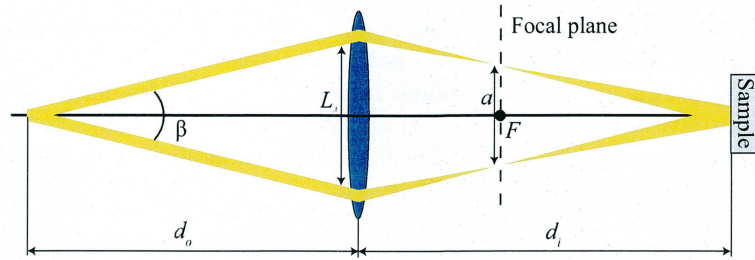


Figure 9: Equivalent imaging scheme using refractive optics.

2.2 Optimization of experimental setup parameters

Before implementing the complex experimental setup it is important to estimate the optimal parameters of the experiment. Because of the complexity of the experiment, there are a number of constraints on the parameters that has to be taken into account. For example the availability of XUV optics is limited (there is only one Schwarzschild objective with particular focal length and transmission spectrum available), laser pulse energy is fixed, the efficiency of harmonic generation that can be achieved and finally spaced constraints in the lab.

First and one of the most important parameter that has to be chosen is the diameter of the XUV pump beam on the sample. Many other parameters that will be discussed in this chapter rely on the selection of the spot size on the sample. The beam must be small so that the refractive index change and diffraction efficiency is high enough to be detected. On the other hand, if the diameter is too small, the divergence of the diffracted probe beam will be too large due to the soft-aperture effect and it will not be possible to capture the diffracted beam efficiently (see Section 2.2.4 for more details).

Second important point to be considered is to make sure that the beams overlap on the sample. To do this, the distances between the gas cell, the objective and the sample have to be calculated. The angle and displacement between two infrared beams is adjusted to satisfy beam overlap condition. The calculations using simple geometrical optics and suggestions how to align the optical setup are described in the Section 2.3.1.

Moreover, the wavelength of XUV beam and the bandwidth is fixed by the properties of the multilayer coating of the available Schwarzschild objective. Although the exact transmission spectrum of the objective has not been measured, it is known that its transmission maximum corresponds to 21st harmonic. However, it also partially transmits adjacent odd harmonics as well which imposes limitations on the maximum angle between harmonic beams due to the available number of interference fringes.

A more detailed discussion on each of the constraint is provided in the following sections of this chapter.

2.2.1 XUV pump beam diameter

The required pump pulse energy density is in the range 10 – 100 mJ/cm² [27]. The energy of the pump pulse at the 21st harmonic was measured to be about $E_p = 0.16 \mu\text{J}$ [28]. The pump pulse energy density J is defined as the pulse energy per unit area S . However, part of the pump pulse energy E_p is lost due to absorption in the aluminum filter (transmission $T_f = 0.5$) and limited reflection of the Schwarzschild objectives coating ($T_o = 0.4$).

$$J = T_f T_o E_p / S \quad (20)$$

For a pump pulse energy density $J = 10 \text{ mJ/cm}^2$, the spot diameter d_s is:

$$d_s = \sqrt{\frac{4E_p T_f T_o}{\pi J}} \approx 20 \mu\text{m} \quad (21)$$

To achieve sufficient pump pulse intensity, the beams must be focused using a high numerical aperture objective.

2.2.2 Estimation of the induced phase-shift of the grating

One of the possible limitations of the proposed induced grating measurement technique is the diffraction efficiency which is mostly determined by the induced refractive index change in the material. A very simple estimation of the induced refractive index change can be done by assuming that every photon of XUV pulse generates one free electron. The number of carriers generated from the XUV pulse of energy E_p is $N = E_p / \epsilon_{ph}$. The carrier density is then $\rho = N / (SL_p)$, where S is the area irradiated by the XUV pulse and L_p is the penetration depth. If pump pulse energy density is $J = E_p / S$, then the carrier density is:

$$\rho = \frac{N}{SL_p} = \frac{E_p}{L_p \epsilon_{ph} S} = \frac{J}{\epsilon_{ph} L_p} \quad (22)$$

The refractive index change Δn can be calculated according to the simple expression:

$$\Delta n = \frac{\rho}{2\rho_c} = \frac{I}{2\rho_c \epsilon_{ph} L_p} \quad (23)$$

where ρ_c is the critical plasma density, defined as $\rho_c = \epsilon_0 m_e \omega_0^2 / q_e^2$ ($q_e = 1.6 \times 10^{-19} \text{C}$ is charge of an electron, $\epsilon_0 = 8.85 \times 10^{-12} \text{C}^2 \text{s}^2 \text{m}^{-3} \text{kg}^{-1}$ is permittivity in free space, and $m_e = 9.1 \times 10^{-31} \text{kg}$ is the mass of an electron). In our case the critical plasma density is $\rho_c = 1.7 \times 10^{21} \text{cm}^{-3}$ at $\lambda_0 = 800 \text{ nm}$ wavelength. What is important for the diffraction efficiency is the accumulated phase shift:

$$\Delta\varphi = \frac{2\pi}{\lambda_0} L_p \Delta n = \frac{J\pi}{\epsilon_{ph} \rho_c \lambda_0} \quad (24)$$

As we see, the accumulated phase shift does not depend on the penetration depth L_p . In case of $J = 10 \text{ mJ/cm}^2$ pulse energy density, we get $\Delta\varphi = 44 \text{ mrad}$

($\sim 1/140$ of the wavelength). However, these estimations do not take into account that the photon may create more than one electron-hole pair. The electron-hole pair creation energy in diamond was found to be about $\epsilon_p = 12$ eV [22]. The photon energy in our case is $\epsilon_{ph} = 32.6$ eV which is more than two times larger than electron-hole creation energy: $\epsilon_{ph}/\epsilon_p = 2.7$.

2.2.3 Estimation of the diffraction efficiency

Diffraction efficiency of the sinusoidal phase grating is given by:

$$\eta = \sin^2 \left(\frac{\Delta\varphi}{2} \right) \quad (25)$$

This leads to $\eta \approx 5 \times 10^{-4}$ diffraction efficiency which is enough for the measurement.

2.2.4 Divergence of the probe beam

There is a limitation on the spot size diameter of the pump beam related to the divergence of the probe beam. The diameter of the diffracted probe beam is approximately the same as the pump beam spot size. For example, if the pump beam is very small, the probe beam will diverge rapidly due to the much longer wavelength. In other words, the XUV pump beam acts as an aperture for the diffracted probe beam. The total angular spread is proportional to the wavelength of the probe pulse and is defined as:

$$\Theta = \frac{2\lambda_0 \sqrt{2 \ln(2)}}{\pi d_s} \quad (26)$$

In case of $\lambda_0 = 800$ nm and beam diameter at half intensity $d_s = 20$ μm the angular spread is 1.7 deg, which is small enough.

2.2.5 Coherence length of the XUV pulse

To achieve efficient high harmonic generation and high temporal resolution ultrashort femtosecond pulses are required. Ultrashort pulses are inherently broadband and the generated high harmonics have also a large bandwidth. The bandwidth is inversely proportional to the coherence length of the pulse. The short coherence length of the high harmonics imposes a limitation for the maximum angle between interfering beams and the area of the interference pattern. The coherence time is defined in terms of the bandwidth:

$$\tau_c = \frac{\lambda^2}{\Delta\lambda} \quad (27)$$

As well known, two broadband point-sources produce an interference pattern limited in width. The fringe period is wavelength-dependent and is different for each spectral component of the broadband pulse. All modes interfere constructively only in the central position and the contrast decreases at the edges. In

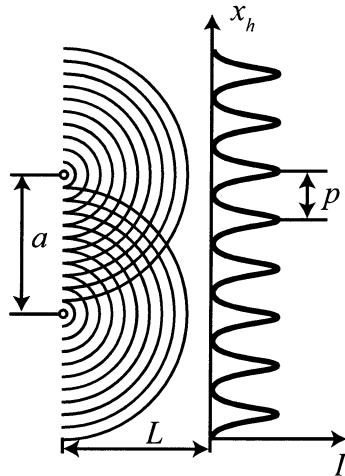


Figure 10: Interference of two point sources.

the case of a rectangular spectral profile of width $\Delta\lambda$, the width of the region between two contrast minima is:

$$L_c = \frac{\lambda^2}{\Delta\lambda} \frac{2L}{a} \quad (28)$$

Here a is the separation of two beam focal points and L is the distance to the screen (multi channel plate detector) as shown in Figure 10. It can be shown that for a given wavelength and bandwidth, there maximum number of visible interference fringes is limited to:

$$N = \frac{L_c}{p} = 2 \frac{\lambda}{\Delta\lambda} \quad (29)$$

where $p = L\lambda/a$ is the interference fringe period. In the following estimations and simulations the bandwidth of 21st harmonic generated in Argon was used which is about 0.2 nm. The short trajectory radiation is used in the experiment, because it is less divergent, narrow-band and has better coherence properties. In that case the maximum number of fringes according to (29) is 380. However, due to a rather broad transmission spectrum of our Schwarzschild objective, adjacent harmonics are also partially transmitted. This reduces the coherence length greatly. If two odd harmonics are taken, then the bandwidth increases up to $\Delta\lambda \approx 3.31$ nm which reduces the number of fringes down to 23, which is still acceptable for our experiment.

2.2.6 Simulation of interference pattern

Simulations were performed to calculate two broadband point source interference patterns. These simulations allow us to understand better our experimental

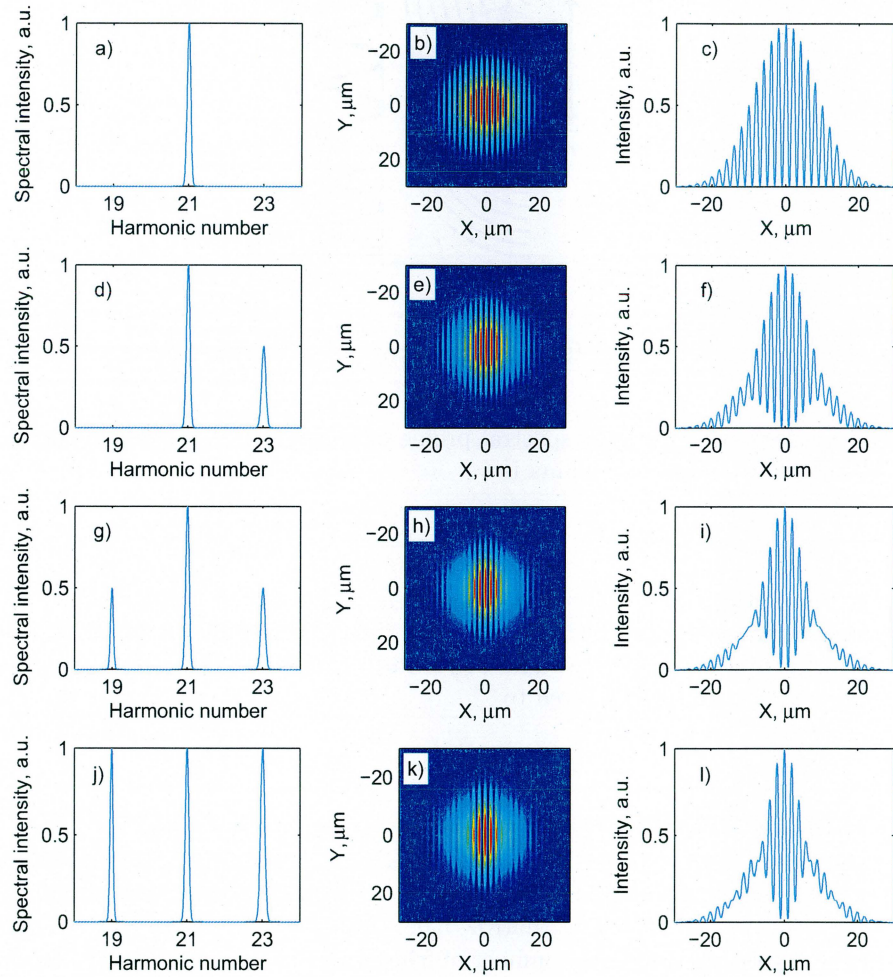


Figure 11: Simulated interference patterns for different number and amplitude of harmonic peaks. Interference fringe period $p = 2\mu\text{m}$, beam diameter $d_s = 20\mu\text{m}$.

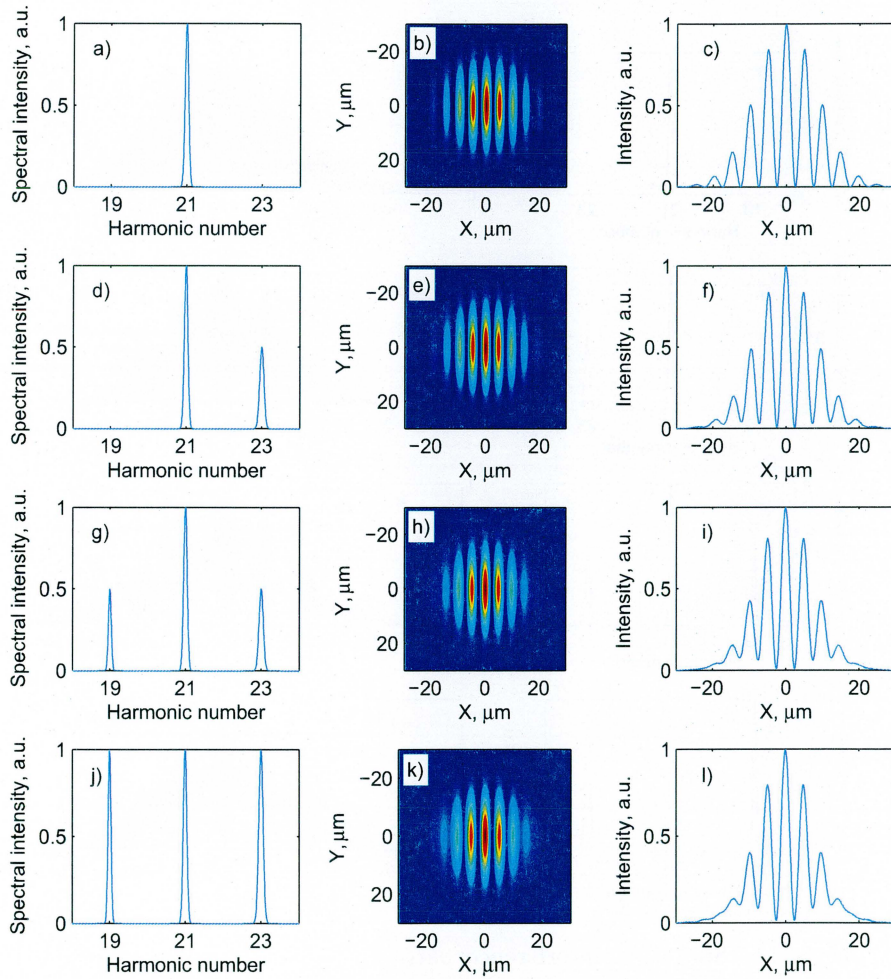


Figure 12: Simulated interference patterns for different number and amplitude of harmonic peaks. Interference fringe period $p = 5\mu\text{m}$, beam diameter $d_s = 20\mu\text{m}$.

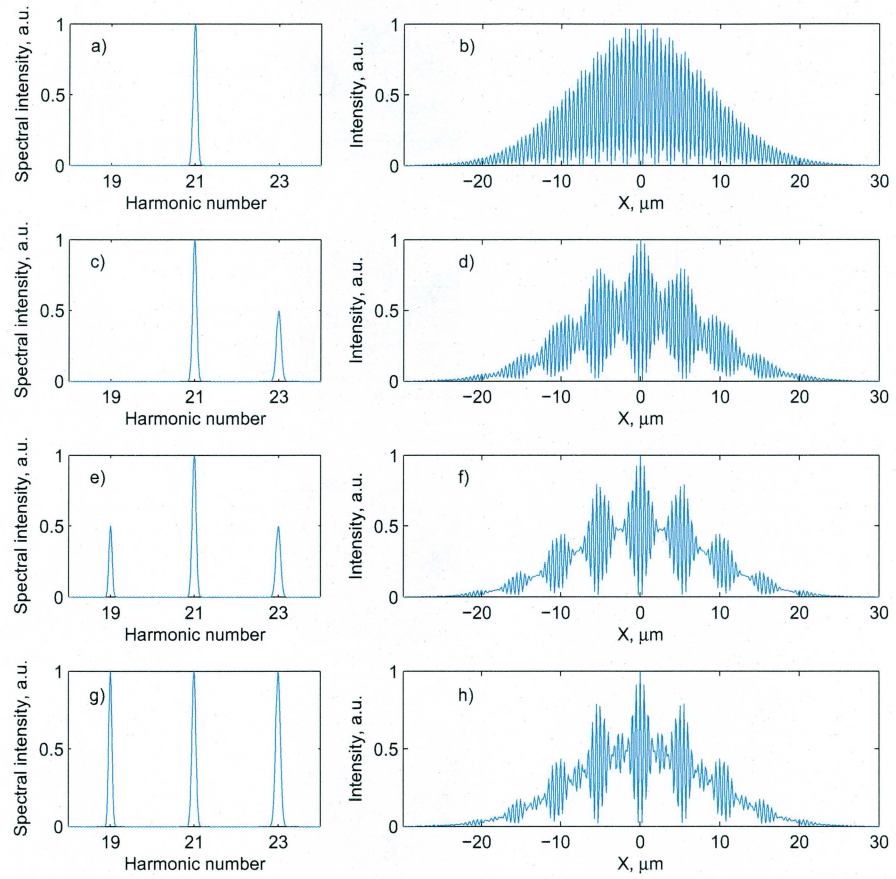


Figure 13: Simulated interference pattern lineouts for different number and amplitude of harmonic peaks. Interference fringe period $p = 0.5 \mu\text{m}$, beam diameter $d_s = 20 \mu\text{m}$.

conditions and to optimize the optical setup parameters. Calculations were done for different number of harmonics and different amplitude ratios, since the exact reflectivity spectrum of the Schwarzschild objective is not known. The spectral shape of each harmonic peak was calculated using a Gaussian line shape of $\Delta\lambda = 0.2$ nm width at half maximum. The resulting radiation spectrum can be estimated as a sum of harmonics spectra centered at λ_0/n and with an amplitude A_n transmitted by the objective:

$$S(\lambda) = \sum_n A_n \exp\left(-4 \ln(2) \left(\frac{\lambda - \lambda_0/n}{\Delta\lambda}\right)^2\right) \quad (30)$$

The total electric field is a superposition of the fields from the two sources, one of whose wavefront is deflected by an angle θ :

$$E(x, y, \lambda) = E_1(x, y, \lambda) + E_2(x, y, \lambda) \exp\left(i\theta \frac{2\pi}{\lambda} x\right) \quad (31)$$

where $E_{1,2}(x, y, \lambda) = \exp(-4 \ln(2) (x^2 + y^2) / d_s^2)$.

The intensity of the broadband interference pattern is the sum of each spectral component:

$$I(x, y) = \int |E(x, y, \lambda)|^2 d\lambda \quad (32)$$

This integral was calculated numerically. The simulations were performed for four different cases that correspond to a single short-trajectory harmonic, two and three odd harmonics of different amplitude ratios as shown in Figure 11 (a), d), g) and j), respectively. Similar simulations with a larger interference period ($p = 5 \mu\text{m}$) are shown in Figure 12. If the interference fringe period is reduced down to $p = 0.5 \mu\text{m}$, beating of multiple harmonics can be observed. This gives a peculiar interference fringe pattern (shown in Figure 13) with characteristic periodic zones of higher interference contrast. The zone width decreases with increasing number of transmitted harmonics and its periodicity is set by the spectral distance between harmonics.

2.3 Optical setup

The general layout of the optical setup is shown in Figure 14. The two beams for HHG are obtained in a Michelson interferometer. An edge of the incoming beam is reflected using a small mirror and is further used as a probe beam. An automatic scan of the delay of the probe pulse in small steps is done by the help of a motorized delay line stage. The pump beam is focused by a spherical mirror of $f_p = 2$ m focal length into a gas cell with 1 mm transverse diameter. The probe and pump pulses are sent off-axis to the sample. This geometry makes it possible to separate the diffraction term easily. A more detailed discussion on different ways to introduce the probe beam is presented in Section 2.3.5.

A thin (180 nm) aluminum filter is used to block the infrared component of the radiation. However, due to interaction with air, the surface is almost

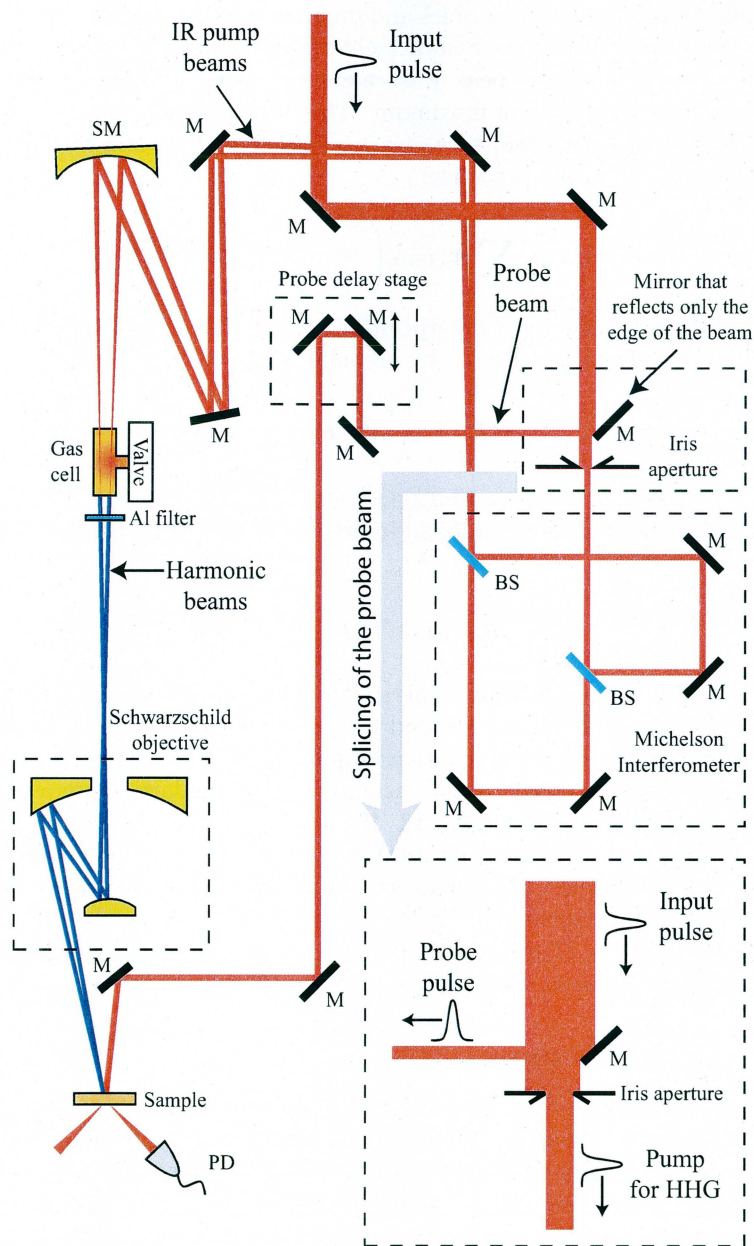


Figure 14: Optical setup of the transient grating pump-probe experiment. M - mirror, SM - spherical mirror, L - lens, BS - beam splitter, F - Aluminium filter, PD - photo diode.

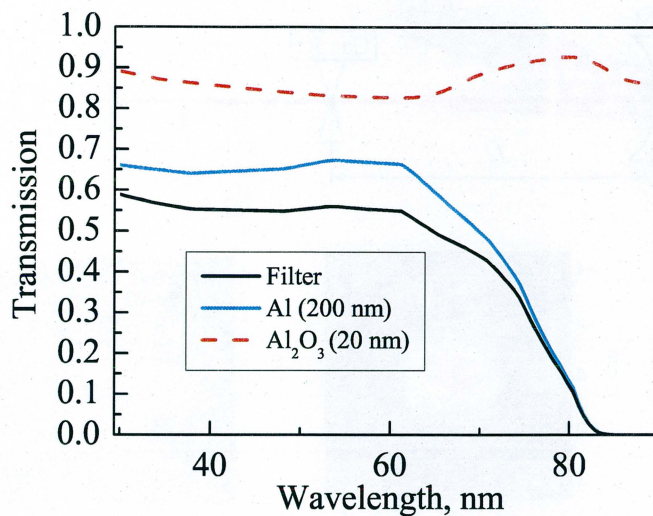


Figure 15: Calculated aluminum filter transmission for 180 nm of Al and 2 nm layer of Al_2O_3 .

immediately covered with $\approx 2 - 10$ nm aluminum oxide layer from both sides. This additional layer highly deteriorates the properties of the filter due to high absorption of the Al_2O_3 in the XUV region.

Because of the requirement of high XUV pulse energy for the experiment, the transmission of the filter is important. It has to be carefully produced just before the measurement keeping it in ambient air as little as possible. To test the maximum achievable transmission of the filter, a new aluminum filter of ≈ 180 nm thickness was produced and its transmission was immediately measured using the experimental setup shown in Figure 16 (a). The generated high harmonic beam is sent through two aluminum filters and imaged using a multichannel plate detector. The second aluminum filter is mounted on a motorized translation stage so that it can be moved in and out of the beam path in the vacuum chamber. A digital CCD camera is used to capture the image to the computer for further analysis. Two images, one measured with just one filter and the second one measured with two filters in the beam path are shown in Figure 16 (b) and (c) respectively. The transmission (ratio of the maximum intensities of the corresponding images) was found to be 55%. The measured value corresponds to the transmission 180 nm of Al and only 2 nm layer of Al_2O_3 . The calculated transmission spectrum of the filter is shown in Figure 15. The measured transmission value fits the calculated transmission spectrum that corresponds to the 180 nm layer of Al and 2 nm layer of Al_2O_3 [29].

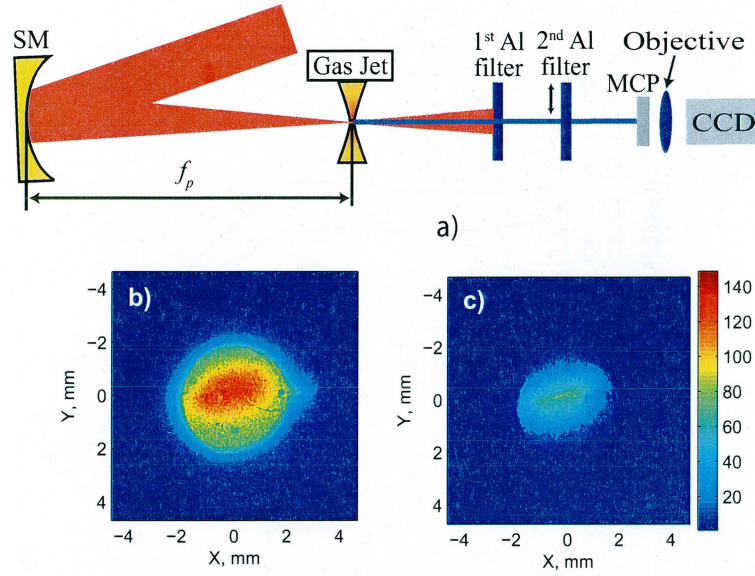


Figure 16: (a) experimental setup for Aluminium filter transmission measurement. (b) and (c) are far-field images without and with filter respectively.

2.3.1 Beam overlap condition

For two beams to interfere, they must be overlapped at the correct position. This is achieved by controlling the angle and the separation of the two generating IR beams. A general optical scheme of our experiment and its parameters is shown in Figure 17. Although in the real experiment, a spherical mirror is used for focusing, in the following discussion based on simple geometrical optics considerations, a lens is used to simplify the explanation. The divergence of the generated XUV harmonic beam is much less than the fundamental IR pump beam as shown in Figure 18 (a). The angle of the two XUV beams depends on the angle θ_p between the two fundamental beams and their separation on the spherical mirror (d_M). Let us discuss two extreme cases. If two parallel pump beams separated by a distance d_M are sent through a lens, the angle of the resulting XUV beams is $\theta = f_p d_M$. On the other hand, if two superimposed pump beams are sent through a lens at an angle θ_p , the resulting harmonic beams also travel at the same angle θ_p as shown in Figure 18 (c). To achieve the desired overlap condition (Figure 18 (d)) both the angle and the separation of the beam must be adjusted, which in the real experiment is done by adjusting the Michelson interferometer. The pump beams must overlap in an intermediate plane (denoted as pump beam overlap plane in Figure 17) between the gas cell and the Schwarzschild objective. The displacement d_M can be measured directly at the focusing mirror. In the experiment the angle between two infrared beams can be precisely deduced from the period p_{ir} of infrared interference fringes:

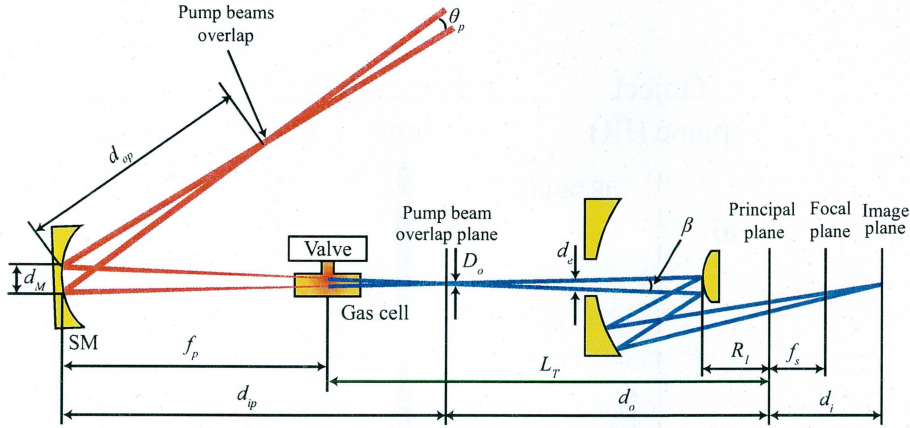


Figure 17: Optical scheme of the pump beams path. SM - spherical mirror.

$\theta_p \approx \lambda_0/p_{ir}$. Note that the imaging concept in this case has to be used carefully. For example even if the IR beams overlap almost entirely before the focusing mirror, the XUV beams may be clearly separated as shown in Figure 18 (e).

Let us derive required the separation and angle and calculate the position of the sample as shown in Figure 19. We begin with an estimation of the distance to the object plane d_o (distance from the principal plane of the Schwarzschild objective to the intermediate plane where pump beams overlap). The d_o is mainly determined by the required spot size d_s . Due to the requirement of a small spot size to obtain a high energy density, the XUV beam cannot be treated as collimated and its divergence must be taken into account. The XUV beam diameter depends on the distance from the gas cell. The angular spread of the input XUV beam was measured to be $\Theta_0 = 0.7$ mrad [30]. Let $L_T = 1.5$ m be the distance from the gas cell to the objective. Then the beam diameter at the distance d_o before the objective is:

$$D_o = (L_T - d_o) \Theta_0 \quad (33)$$

The magnification to get the required spot size is $M = d_s/D_o$. On the other hand, from the imaging equation:

$$\frac{1}{f_s} = \frac{1}{d_i} + \frac{1}{d_o} \quad (34)$$

and from the definition of magnification $M = d_i/d_o$ we find the distance where the beams must overlap:

$$d_o = \frac{L_T \Theta_0 + d_s}{\Theta_0 + d_s/f_s} \quad (35)$$

The parameter d_i is the distance from the principal plane of the Schwarzschild objective to the image plane where sample is placed:

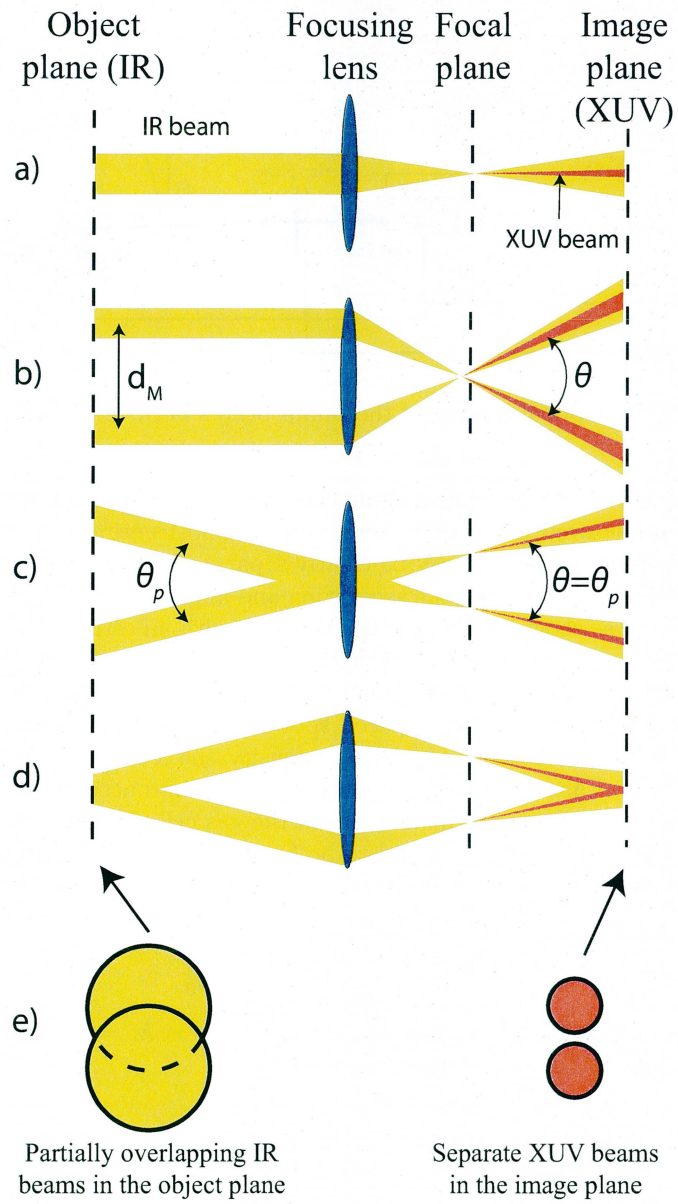


Figure 18: Illustration of the influence of the separation and the angle between two IR pump beams on the angle and overlap of the generated XUV beams.

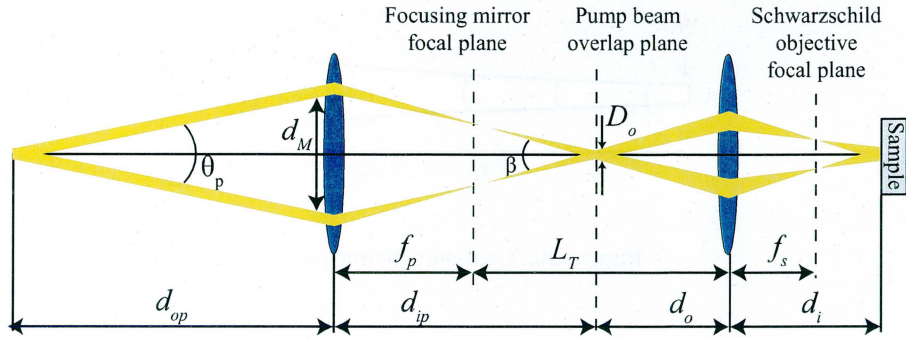


Figure 19: Notation used for the two beam overlap condition.

$$d_i = \frac{f_s d_o}{d_o - f_s} \quad (36)$$

For a spot size $d_s = 20 \mu\text{m}$ and with a focal length of the Schwarzschild objective $f_s = 26.9 \text{ mm}$, we find that $d_o = 741 \text{ mm}$ (the beams overlap approximately 75 cm before the objective). According to (36), the sample must be placed $d_i - f_s = 1.0 \text{ mm}$ out of the focal plane.

The next step is to express the condition for the pump beams to overlap in the intermediate plane. The pump beam overlap condition is given by the imaging formula:

$$\frac{1}{f_p} = \frac{1}{d_{op}} + \frac{1}{d_{ip}} \quad (37)$$

The distance from the spherical mirror to the intermediate pump beam overlap plane d_{ip} is given by distances L_T and d_o (35): $d_{ip} = f_p + L_T - d_o = 2.76 \text{ m}$.

2.3.2 Estimations of Gaussian beam parameters

To verify the above-mentioned simple estimations based on geometrical optics, a more exact analysis based on Gaussian beam transformation was carried out. To describe a Gaussian beam, a complex beam parameter is used: $q = z + iz_r$. The Rayleigh length of the generated XUV beam is $z_{r1} = \frac{\lambda_p}{\theta_0^2 \pi} = 98.7 \text{ mm}$, where $\theta_0 = \Theta_0/2 = 0.35 \text{ mrad}$ is the divergence angle (half of the full angular spread). According to its definition the beam parameter of the initial beam at the objective is:

$$q_1 = L_T + iz_{r1} \quad (38)$$

Transmission through a lens is described as a transformation to another Gaussian beam with complex parameter q_2 (see Figure 20 for more details), where:

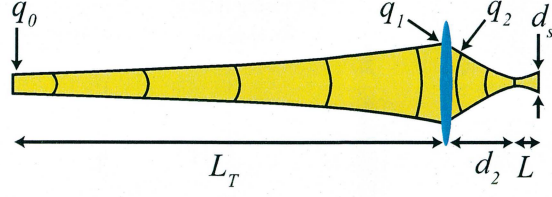


Figure 20: Gaussian beam parameters.

$$\frac{1}{q_2} = \frac{1}{q_1} - \frac{1}{f_s} \quad (39)$$

The real part of the parameter q_2 describes the distance from the lens to the waist $d_2 = |\text{Re}(q_2)|$.

$$d_2 = \left| \frac{f_s^2 L_T - L_T^2 f_s - f_s z_{r1}^2}{(f_s - L_T)^2 + z_{r1}^2} \right| = 27.39 \text{ mm} \quad (40)$$

Also the distance from the waist to the sample is calculated using the beam radius formula:

$$L = z_{r2} \sqrt{\left(\frac{d_s/2}{w_{02}} \right)^2 - 1} = 0.52 \text{ mm} \quad (41)$$

where $z_{r2} = \text{Im}(q_2) = 33 \text{ } \mu\text{m}$ and $w_{02} = \sqrt{\frac{\lambda_h z_{r2}}{\pi}} = 0.63 \text{ } \mu\text{m}$ are the Rayleigh length and waist radius of the beam after objective. The distance from the sample to the focal plane is $L + d_2 - f_s = 1.0 \text{ mm}$. The results of the Gaussian beam analysis correspond well with the simple geometric optics case discussed in the section above, because the condition $L \gg z_{r2}$ is fulfilled.

2.3.3 Angle between the pump beams

The angle between the two XUV beams is mainly determined by the required fringe period p and the beam diameter d_s on the sample. The optimal interference fringe period is selected also according to the pump beam diameter ($d_s = 20 \text{ } \mu\text{m}$) and the number of fringes available ($N \approx 20$). The simulations of interference pattern presented in Section 2.2.6 suggest that the optimal interference fringe period p is about $2 \text{ } \mu\text{m}$. The period of the grating corresponds to an angle of diffraction of the probe beam ($\lambda_0 = 0.8 \text{ } \mu\text{m}$) of $\approx 23^\circ$ which is large enough for easy detection. From the interference fringe period the angle between two XUV beams can be estimated using the following formula:

$$\beta = \frac{L\lambda_h}{f_s p} \quad (42)$$

where $L = 0.52$ mm is the distance from the waist to the sample. According to the parameters of our experimental setup, the angle β is 0.37 mrad.

Secondly, the angle between the two IR pump beams θ_p can be expressed in terms of the angle between the two harmonic beams β and d_{ip} . From geometrical optics, the ratio between these two angles is simply $\theta_p = \beta d_{ip}/d_{op}$. By substituting the d_{op} from (37) we find:

$$\theta_p = \beta(d_{ip} - f_p)/f_p = 0.14 \text{ mrad} \quad (43)$$

From this angle we also find that the focal point separation in the gas cell is small enough:

$$d_g = \theta_p f_p = 0.28 \text{ mm}, \quad (44)$$

since it is smaller than the inner diameter of the gas cell. It is convenient to align the angle between the two pump beams θ_p according to the fringe period of the IR interference pattern. The angle θ_p according to (43) gives an interference fringe period in the IR $p_{ir} \approx \lambda_0/\theta_p = 5.8$ mm. Another parameter to be adjusted is the separation between the two beams at the spherical HHG pump mirror:

$$d_M = d_{op}\theta_p = 1.0 \text{ mm} \quad (45)$$

The beam walk-off (distance between the centers of the two beams) at the input aperture of the Schwarzschild objective is much less than its clear aperture:

$$d_e \approx \beta d_o = 0.27 \text{ mm} \quad (46)$$

2.3.4 Diffraction simulation

As it was pointed out in Section 2.2.5, the number of fringes is relatively small due to the large bandwidth of the XUV pump pulse. Moreover, the contrast of the fringes is modulated due to the Gaussian intensity distribution of the pump pulse. To test the effects of diffraction related to the complexity of the induced grating a simple simulation was performed and the results are shown in Figure 21. The probe beam diameter was selected to be two times larger than the pump pulse diameter. Corresponding phase grating was calculated from the simulated interference pattern shown in Figure 11 k). Low and high diffraction efficiency cases were considered. In the high diffraction efficiency case one can see the depletion of the DC term (non-diffracted light) in the center of the beam.

Note that these simulations are only intended to test the effects due to limited number of interference fringes. The experimental conditions lead to computational problems due to relatively large diffraction and beam divergence angles. Therefore, a scaling was applied to perform a diffraction calculation.

2.3.5 Probe beam path

There are three different ways to send the probe beam through the induced transient diffraction grating as shown in Figure 22. The collinear probe beam

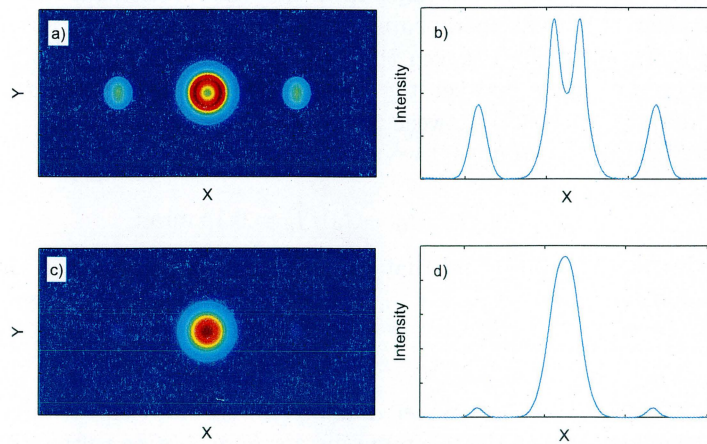


Figure 21: Diffraction simulation results. (a) and (b) cases correspond to high diffraction efficiency. (c) and (d) cases correspond to low diffraction efficiency.

geometry shown in Figure 22 (a) has two main advantages. First, the temporal resolution is not reduced because the pump and the probe pulses completely overlap in space. Secondly, the alignment is relatively easy and robust. There is no need to worry about spatial overlap of the pulses in the sample. The alignment of the temporal overlap of the pump and probe pulses can be done by looking for the interference of two pulses or second harmonic generation in an autocorrelator. However, this configuration has one major disadvantage: the probe beam after the objective is divergent. This makes it somewhat difficult to separate the diffraction orders. This can be partially avoided by limiting the input probe beam diameter to a small diameter using an aperture. A reasonably small (less than 3°) divergence angle can be achieved with a 1 mm beam diameter. Another disadvantage is varying intensity with the position of the sample. It is easy to destroy the sample by putting it too close to the focus of the objective beam.

In the off-axis probe beam geometry a small mirror is placed just after the Schwarzschild objective as depicted in Figure 22 (b). The main advantage of this configuration is that the probe beam is collimated which makes it easy to select the single diffraction maximum and block the non-diffracted light. Because no intense infrared light is sent through the objective, there is no risk of damaging the objective. However, pump and probe pulses arrive to the sample slightly at an angle which prevents them from overlapping in space as shown in Figure 23. The minimal angle that can be achieved is approximately $\theta_{pr} \approx 4^\circ$. If we assume that the diameter of the induced transient grating is $d_s = 10 \mu\text{m}$ (see Section 2.2.1 for details), then the deterioration of temporal resolution is acceptable for the dynamics we want to study: $\Delta t \approx \theta_{pr} d_s / c = 4.4 \text{ fs}$.

It is also possible to make the probe beam counter-propagating to the pump pulse as shown in Figure 22 (c). This arrangement combines merits of collinear and off-axis configurations. The probe beam can be easily sent collinearly to the pump beam which does not impose a limitation on the temporal resolution. The XUV radiation of the pump pulse is absorbed in a thin (≈ 50 nm) layer, so the deterioration of temporal resolution due to counter-propagating pulses is negligible (≈ 0.2 fs). However, this configuration has a serious disadvantage: the relatively strong non-diffracted probe beam goes to the objective which is focused by the concave mirror close to the convex mirror surface (≈ 1.2 cm) which might easily be damaged.

To summarize the discussion above, the most appropriate configuration in our case turned out to be the off-axis one.

3 Experimental setup

3.1 The Terawatt laser system

The high-power laser used in our experiment is based on chirped pulse amplification (CPA) technique [31]. This technique allows achieving intensities up to 10^{18} W/cm² with a table-top laser system. The terawatt laser system (shown in Figure 24) used in this experiment delivers pulses of 30 fs duration at 800 nm wavelength at a repetition rate of 10 Hz. For high harmonic generation a low-power arm which delivers a pulse with 90 mJ energy (≈ 180 mJ before compression) is used. The beam diameter is approximately 50 mm. The actual pulse energy used in the experiment is much smaller and is adjusted by blocking part of the beam using a variable diameter aperture. Finally, only about a few mJ of infrared pulse energy is used to generate high harmonics.

To avoid gain-narrowing of the pulse spectrum during amplification, an acousto-optic programmable dispersive filter (AOPDF) is used to make a dip in the spectrum of the oscillator seed pulse. The spectrum of the amplified pulse is shown in Figure 25.

3.1.1 Pump pulse characterization

High harmonic generation of reasonable efficiency can only be achieved with ultra-short laser pulses [14]. Therefore, adjustment of the laser is a crucial part in our experiment. Longer pulses ionize the atoms of the high harmonic generation medium and no neutral atoms are exposed to the peak intensity of the pulse. Laser pulses were characterized using the Frequency Resolved Optical Gating (FROG) technique. FROG is an autocorrelator combined with a spectrometer. An iterative algorithm is used to match the pulse model to the measured spectrum at different time delays (so-called FROG trace). This technique is capable of measuring the ultra-short pulse duration and spectral phase. For the measurement we used a device called “Grating-eliminated no-nonsense observation of ultra-fast incident laser light e-fields” (GRENOUILLE) that has no moving parts. To measure the spectrum and achieve an auto-correlation

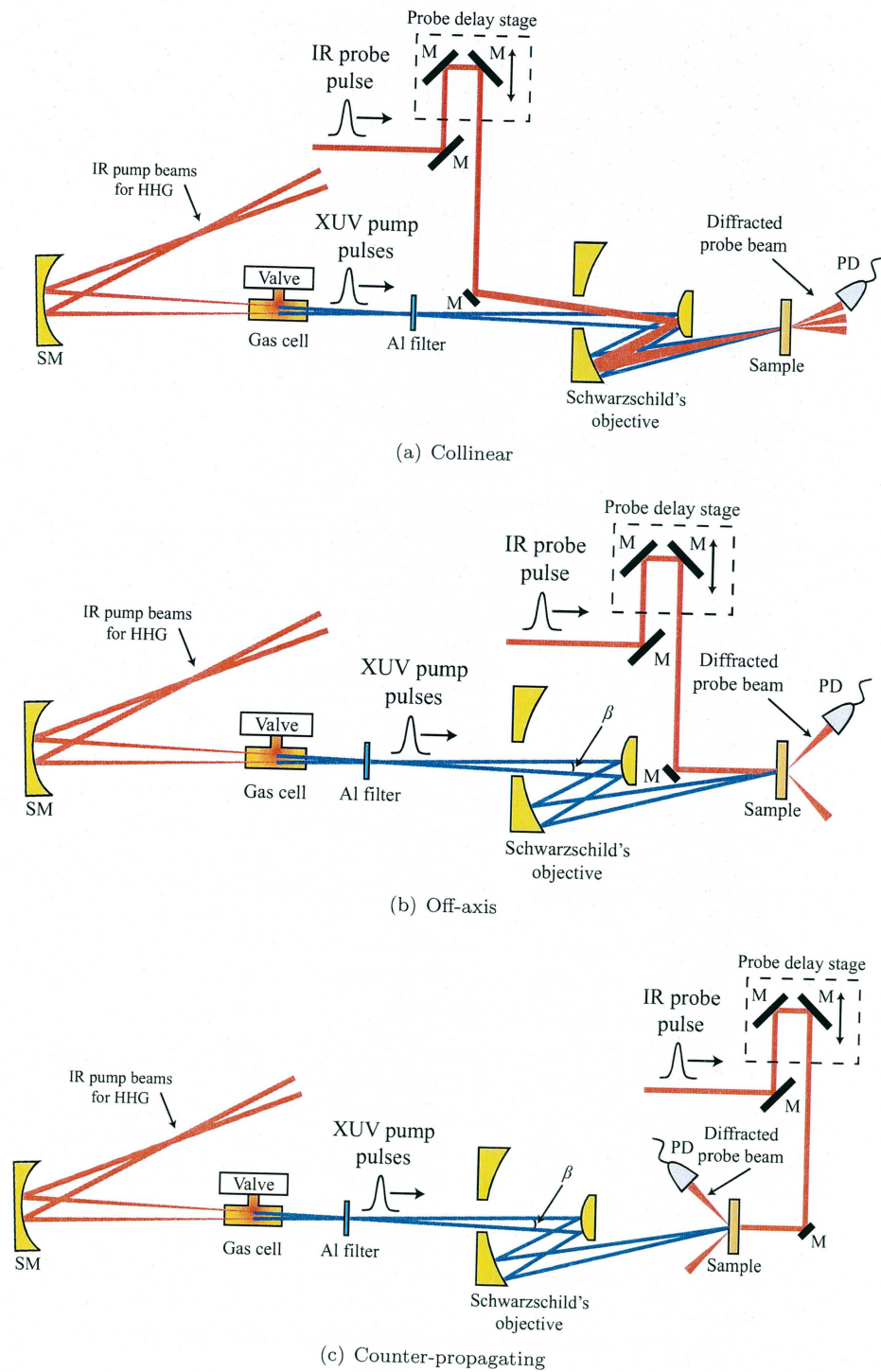


Figure 22: Three different probe beam configurations.

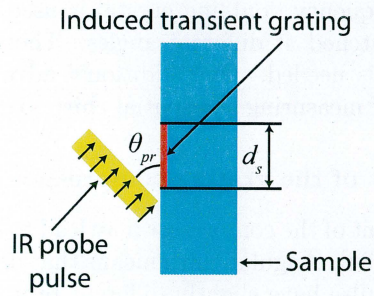


Figure 23: Illustration of the reduction of temporal resolution due to non-collinear pump and probe pulses.

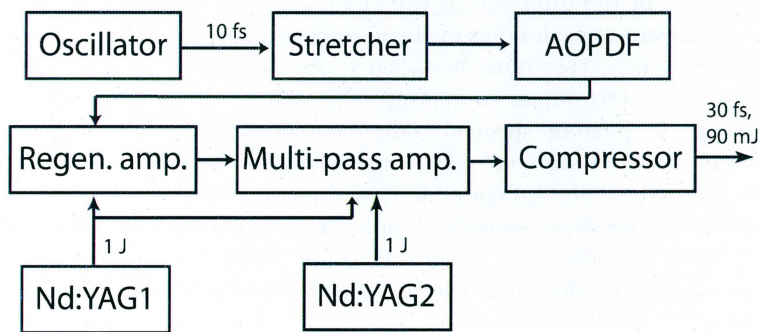


Figure 24: The schematic of the Terawatt laser system.

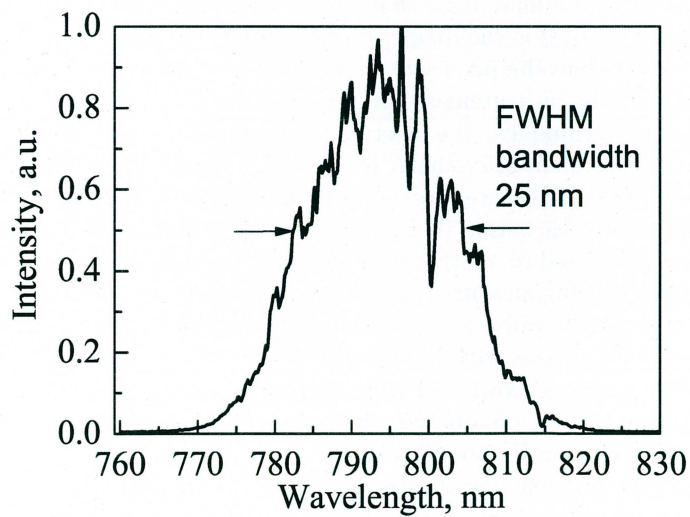


Figure 25: A spectrum of the Terawatt laser pulse.

function a thick frequency doubling crystal is used. Different spectral components are phase matched at different angles. Therefore no dispersive element (grating or prism) is needed. One additional advantage of GRENOUILLE is that it is capable of measuring the spatial chirp [32] and pulse front tilt [33].

3.1.2 Alignment of the grating compressor

A slight misalignment of the compressor may lead to big changes in angular chirp and pulse duration [34]. Angular chirp means that different spectral components of the ultra short pulse have slightly different propagation directions. When a laser pulse with significant angular chirp is focused using a lens, the different spectral components arrive at different lateral positions. Two phenomena occur that ultimately lead to intensity reduction in the focus. First, the focal point is elongated in the direction of the angular chirp. Second, the bandwidth becomes narrower at each point of the focus leading to temporal pulse broadening. Therefore, special care must be taken while aligning the compressor.

One of the techniques to measure the angular dispersion is a far-field measurement. If different spectral components travel at slightly different angles, they will arrive at different lateral positions in the focus of the lens and the beam spot size will be elongated in that direction. However, this method turned out to be not sensitive enough. Moreover, it is affected by the beam intensity distribution imperfections. The sensitivity of such a measurement is limited by the angular resolution of the imaging setup which is given by the Rayleigh criterion:

$$\sin(\theta) = 1.22 \frac{\lambda_0}{D} \quad (47)$$

where θ is the minimal angle that can be resolved, λ_0 is the central wavelength of the pulse and D is the diameter of the input beam. Note that once the spot size is larger than the pixel size of the camera, increasing the focal length does not improve the measurement precision.

Another technique is the inverted field interferometer [34]. The basic optical scheme of such an interferometer is shown in Figure 26 (a). The basic idea of the method is that pulse interferes with its flipped replica. A retroreflector is used in one arm of a Michelson interferometer and a single mirror at almost 0° angle of incidence is used in another arm. A small angle in the vertical (different than that which is being measured) direction is introduced so that interference fringes are visible. If the pulse is tilted and the delay between two pulses is adjusted appropriately, fringes with high contrast will be visible only in a narrow stripe across the pulse as shown in Figure 26 (b). Once the compressor is aligned and the angular chirp is eliminated, the pulse can be perfectly overlapped with its replica as shown in Figure 26 (c).

The measurement results using the inverted field interferometer are shown in Figure 27. A computer program was written that captures the interference pattern and calculates contrast of the image in the vertical direction in real time. A quantitative measure of contrast is given by:

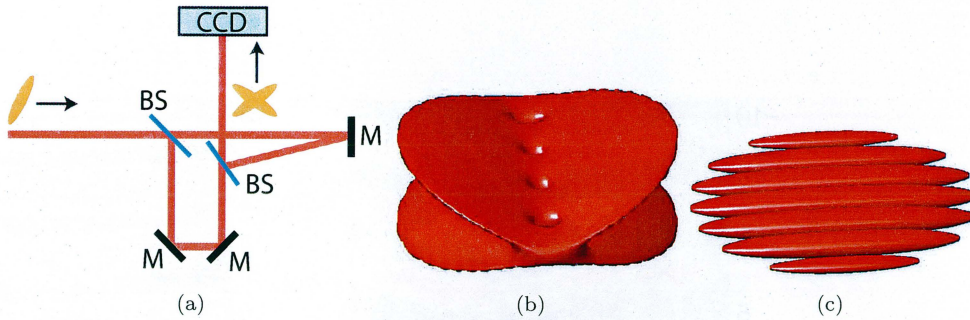


Figure 26: Schematic of an inverted field autocorrelator. (a) basic optical setup, (b) interference of tilted pulses (uncompensated angular dispersion), and (c) interference of a non-tilted pulse.

$$V(x) = \frac{I_{max}(x) - I_{min}(x)}{I_{max}(x) + I_{min}(x)} \quad (48)$$

where $I_{max}(x)$ and $I_{min}(x)$ are the maximum and minimum intensities in the lineout of the image at position x .

3.1.3 Pulse duration measurement

Pulse duration and temporal chirp were measured using the FROG technique. Figure 28 shows the comparison between the measured FROG trace and the simulation based on an iterative algorithm.

The minimal (also sometimes referred as transform limited) pulse duration for Gaussian-shaped pulses is given by the relation:

$$\tau_{min} \simeq \frac{0.44}{\Delta\nu} \quad (49)$$

where $\Delta\nu$ is the bandwidth of the pulse. To achieve the minimal pulse duration, the temporal chirp of the pulse must be compensated. The chirp of the pulse is adjusted by changing the distance between the gratings of the compressor. Pulse shape and temporal and spectral phase of the pulse after compressor alignment retrieved from the model are shown in Figure 29. The duration of the pulse was 55 fs, which is longer than expected. This is caused by the relatively narrow (≈ 15 nm full width at half maximum) bandwidth of the pulse during the pulse duration measurement. After adjustment of the AOPDF, the bandwidth was increased up to 25 nm as shown in Figure 25 and the pulse duration is now expected to be ≈ 33 fs.

3.2 The flat field spectrometer

The harmonic spectrum was observed using the flat-field spectrometer. Its basic optical schematic is shown in Figure 30. The spectrometer consists of a

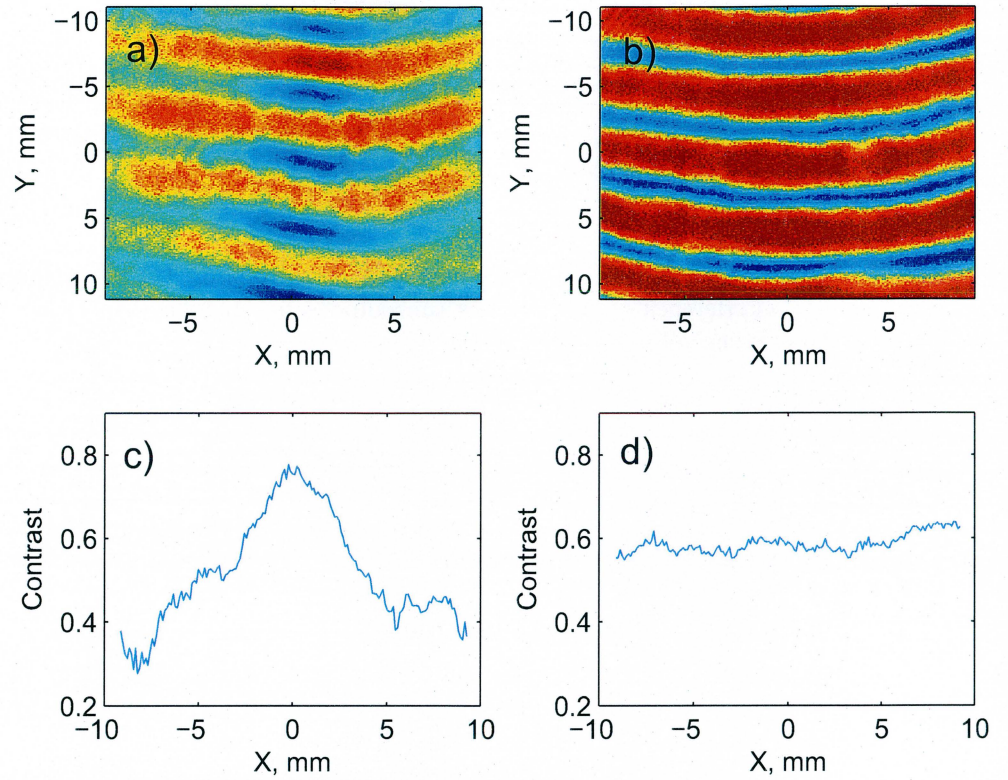


Figure 27: Inverted field interferometer measurement results. Before alignment of the compressor, the interference pattern and the corresponding contrast curve shown in (a) and (c), respectively, clearly show the presence of pulse front tilt. After adjusting the compressor, the uniform contrast interference fringes are visible in (b) and (d).

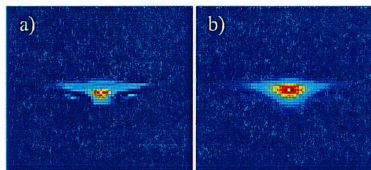


Figure 28: FROG trace: (a) measured, (b) retrieved using an iterative algorithm.

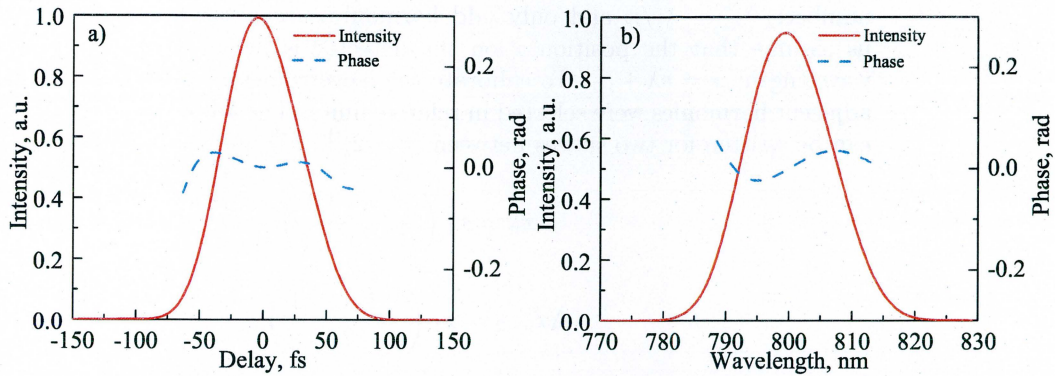


Figure 29: FROG measurement data: (a) retrieved temporal pulse shape and temporal phase, (b) retrieved spectrum and spectral phase of the pulse.

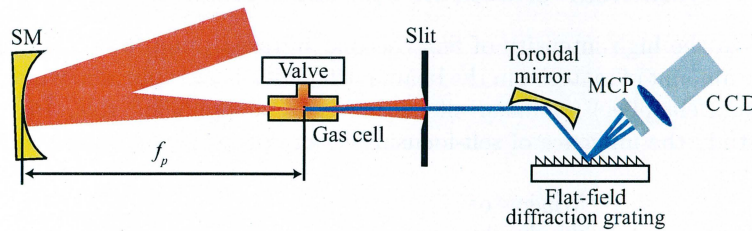


Figure 30: A basic schematic of the flat-field XUV spectrometer.

$\approx 200 \mu\text{m}$ entrance slit, a toroidal mirror, a reflection diffraction grating and a multi-channel plate detector (MCP). The entrance slit is located approximately at a 2 m distance from the gas cell. The focusing optical setup and the gas cell are the same as in the main experimental setup shown in Fig 14. A software program based on LabVIEW records spectrum using a digital computer camera and processes it. A special diffraction grating with varying period is used to image the spectrum onto the flat detector. Because of the relatively long distance between the gas cell and the slit, effectively a far field is imaged by the spectrometer. This makes it possible to measure the far-field spatial profile (divergence) of different harmonics. The resolution of the spectrometer is estimated to be 0.2 nm.

3.2.1 The calibration of the spectrometer

The position on the detector (MCP) must be calibrated in order to get the correct wavelength scale. Fortunately, no additional measurement is needed and the calibration information can be extracted from the measured HHG spectrum itself. The reason is that a priori information is known about the HHG spectrum: the wavelength of each harmonic λ_n is inversely proportional to the harmonic

number: $\lambda_n = \lambda_1/n$ and only odd harmonics are present in our case. Let us assume that the position x on the detector is linearly dependent on the wavelength: $x = c\lambda + c_0$. To calibrate the spectrometer the positions of three adjacent harmonics were selected in relative units. The following set of equation can be written for two spaces between $(n-2)^{\text{th}}$, n^{th} and $(n+2)^{\text{th}}$ harmonics:

$$\Delta x_n = x_1 \left(\frac{1}{n} - \frac{1}{n+2} \right) \quad (50)$$

$$\Delta x_{n-2} = x_1 \left(\frac{1}{n-2} - \frac{1}{n} \right) \quad (51)$$

The harmonic number can then be expressed as $n = 2(a+1)/(a-1)$, where $a = \Delta x_{n-2}/\Delta x_n$.

3.3 Nonlinear effects in optical elements

Due to the high intensity of femtosecond infrared pump pulses and the rather large amount of material in the beam path (thick beam splitters, window into the vacuum chamber) nonlinear effects may play a significant role. In this section we study the influence of self-focusing in an optical element.

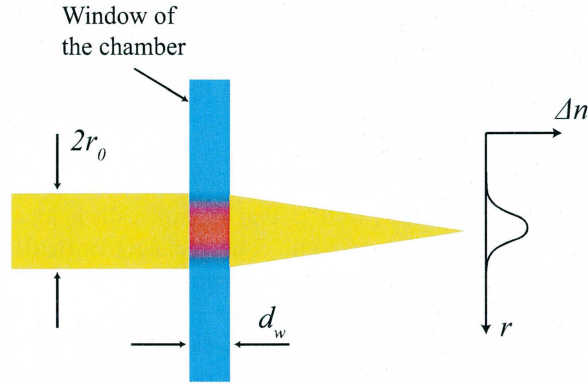


Figure 31: Self-focusing of the beam in the window of the chamber.

The beam profile can be approximated using a quadratic expression:

$$I(r) \approx I_0 \left(1 - \frac{r^2}{r_0^2} \right) \quad (52)$$

where I_0 is the peak intensity, which can be expressed in terms of pulse energy E_p , pulse duration τ_0 and beam radius r_0 :

$$I_0 = \frac{E_p}{\tau_0 \pi r_0^2} \quad (53)$$

Due to the Kerr effect, the induced phase shift is then proportional to the intensity-dependent refractive index n_2 :

$$\Delta\varphi(r) = I(r)n_2k_{IR}d_w \quad (54)$$

where $k_{IR} = 2\pi/\lambda_{IR}$ is the wave number of the laser and d_w is the thickness of the optical element. The effect can be compared to the phase-shift induced by a lens of focal length f_{nl} within the paraxial approximation:

$$\Delta\varphi(r) = k_{IR}r^2/f_{nl} \quad (55)$$

From this we find that the nonlinear focal length is:

$$f_{nl} = \frac{r_0^2}{2n_2d_wI_0} \quad (56)$$

By substituting expression (53) to (56) we find that $1/f_{nl} \propto r_0^4$. If the original focal length of the focusing mirror is f_p and distance to the window is L_w , then the focus position (with respect to the focusing mirror) of the combined two lens system is:

$$f_e = f_{nl} + L_w - \frac{f_{nl}^2}{f_p + f_{nl} - L_w} \quad (57)$$

Let us estimate the shift of the focus at the gas cell due to self-focusing in the window of the chamber. The window of the chamber is made of BK7 glass of thickness $d_w = 1$ mm and is located approximately $L_w = 30$ cm away from the window of the focusing mirror. The intensity-dependent refractive index of BK7 is $n_2 = 3.4 \times 10^{-16} \text{cm}^2/\text{W}$ [35]. The intensity that corresponds to a pulse energy $E_p = 10$ mJ of duration $\tau_0 = 35$ fs and 10 mm beam diameter at the window of the chamber ($r_0 = 5$ mm) is $I_0 = 3.6 \times 10^{11} \text{W}/\text{cm}^2$. According to (56) the nonlinear focal length is rather long $f_{nl} \approx 100$ m. However, the shift of the focus calculated according to (57) $\Delta f = f_p - f_e = 2.8$ cm is non-negligible. The accumulated phase shift due to intensity dependent refractive index (so-called B-integral) is $B = n_2I_0d_wk_{IR} = 0.97$ rad which implies that nonlinear effects may play a role in the optical setup. A plot of the shift of focus and of the intensity as a function of beam diameter is shown in Figure 32. These estimations suggest that nonlinear effects impose a limitation that prevents increasing the intensity of the infrared pump beam.

4 Results

4.1 The measurement of HHG spectrum

A typical spectrum of the generated high harmonics to be used in the experiment is shown in Figure 33. It was measured using the flat field spectrometer described in section 3.2. The cut-off can be seen at 27th harmonic. The 21st

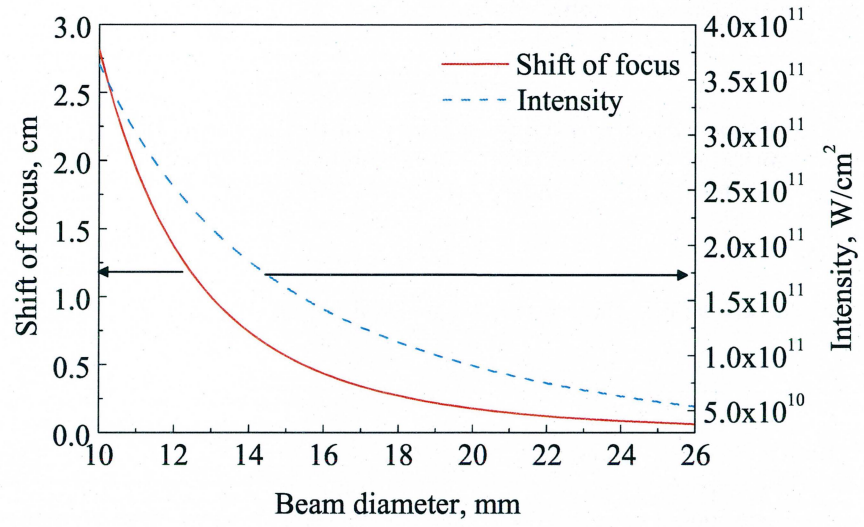


Figure 32: Shift of focus due to self-focusing in the window to the vacuum chamber.

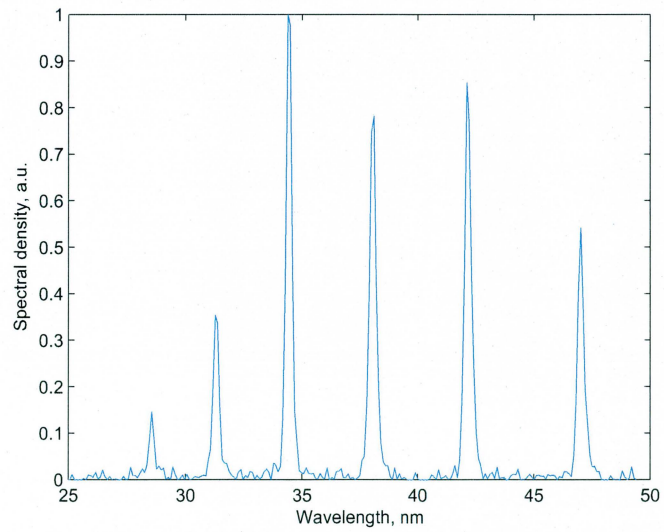


Figure 33: Measured spectrum of the generated high harmonics.

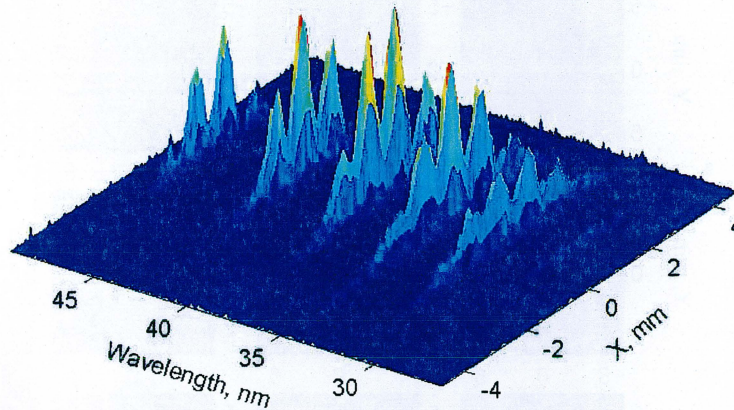


Figure 34: Two harmonic beam interference measurement using a XUV spectrometer.

harmonic peak that corresponds to the peak transmission of the Schwarzschild is intense, although less than the 19th and 23rd.

The spectrometer is built in such way that the entrance slit is imaged onto the detector. The entrance slit is placed at a 2 m distance from the gas cell, which is much larger than the Rayleigh length of the harmonic beam. This effectively makes it possible to measure the spatial profile of the beam in the far-field in one dimension and the wavelength in the other dimension. This property of the spectrometer was used to observe the fringes of two harmonic beam interference pattern. The spectrometer separates each harmonic in space, therefore the high contrast fringes can be achieved. In order to test the two coherent harmonic beam generation in our setup, two infrared pump beams were focused to the gas cell at an angle. The measured $r - \lambda$ spectrum is shown in Figure 34. The high contrast interference fringes were successfully obtained.

4.2 Far-field measurements

A sequence of far-field measurements was performed to study the beam properties as a function of high-harmonic generation parameters. The intensity of the XUV beam was captured using a multi channel plate detector and a CCD camera. The XUV beam was sent through the Schwarzschild objective to filter the bandwidth so that only the harmonics that are actually used in experiment were measured. One aluminum filter was used to block the infrared radiation and the Schwarzschild objective was placed after the filter (≈ 20 cm before the multichannel plate detector).

First, the effect on the high-harmonic generation efficiency due to reduced IR pump beam intensity was studied. For two XUV beam generation, the Michelson interferometer was used to split laser beam into two beams as shown in

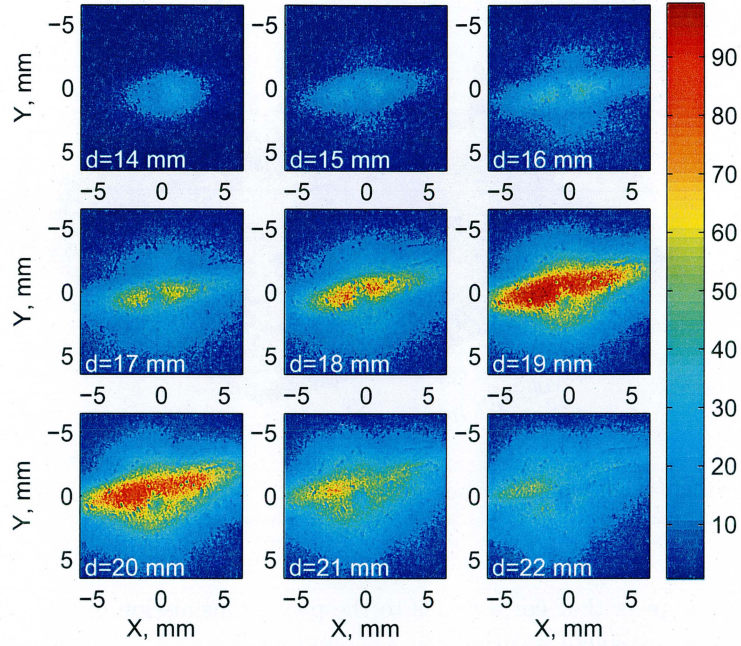


Figure 35: Far field intensity profiles of XUV beam generated using the full IR beam intensity.

Figure 14. However, the intensity of each beam is only a quarter of the incoming beam which might affect the highly non-linear high harmonic generation process. A sequence of far field XUV beam profiles at different input beam diameters (adjusted using a variable diameter iris aperture) is shown in Figure 35. Increasing the aperture diameter increases the intensity in the focus of the beam, because a larger amount of energy is transmitted through the aperture and the beam is focused more tightly due to the larger beam diameter. The XUV beam shape looks distorted most likely due to off-axis focusing of the IR beam with a spherical mirror and nonlinear effects in the optical elements. The maximum beam intensity is acquired for an input beam diameter $d = 19$ mm. Further increase of the IR beam intensity does not improve the high harmonic generation efficiency.

Far field beam profiles acquired using a quarter of IR beam intensity are shown in Figure 36. The beam was sent through the Michelson interferometer and one arm was blocked. Comparing to the full intensity case, the XUV beam intensity dropped by a factor of 4 for an optimal input diameter $d = 16$ mm. The optimal diameter of the input beam has decreased comparing to the full intensity case. This observation is counterintuitive, because in order to reach the same intensity in the focus with the smaller intensity of the input beam would require focusing it more tightly. We attribute this discrepancy to the nonlinear

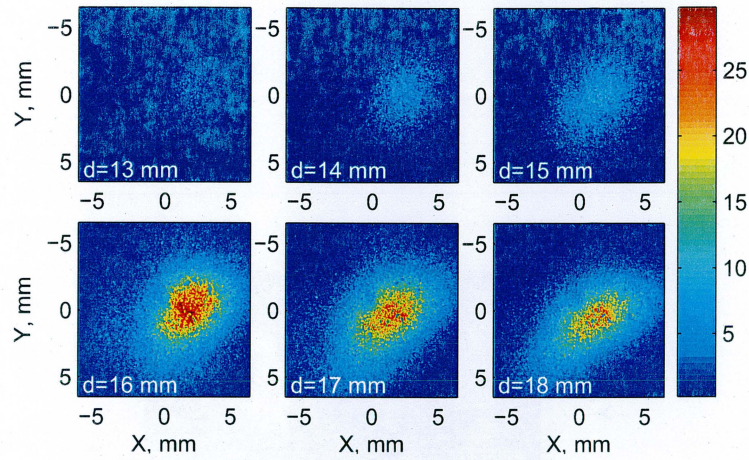


Figure 36: Far field intensity profiles of XUV beam generated using a quarter of the IR beam intensity.

effects in optical elements and air. The self phase modulation effects described in Section 3.3 are highly intensity dependent and therefore they are insignificant when intensity is decreased by a factor of 4. The shape of the generated XUV beam is also much more regular in case of quarter of IR beam intensity.

Moreover, two independent XUV beam generation was tested. Firstly, each interferometer arm was aligned and high harmonic generation was tested by sending the beams to the generation chamber one beam at a time. Two XUV beams of similar intensity were acquired as shown in Figure 37 (a) and (b). The two IR beams were displaced (as explained in Section 2.3.1) so that the XUV beams do not overlap before the Schwarzschild objective. Finally, two XUV beams generated using both interferometer arms are shown in Figure 37 (c). Also, the maximum angle between the IR pump beams was measured: $\max(\theta_p) = 0.27$ mrad, which corresponds to a focal point separation of $540 \mu\text{m}$ in the gas cell. There is also some certain minimal angle between the two beams, because the spots must not overlap in the gas cell so that high-harmonic generation of the two beams is independent.

4.3 Interference fringe pattern measurement

Finally the interference pattern of two XUV beams was measured. The XUV beams were overlapped on the detector and the delay between infrared pump beams was adjusted to get the maximum contrast. The interference pattern and the corresponding lineout are shown in Figure 38. This result shows that it is possible to get a high interference fringe contrast using multilayer narrowband XUV optics and to avoid using a grating.

The angle between the two infrared beams was chosen in order to achieve high contrast of the interference fringes while keeping as many fringes as possi-

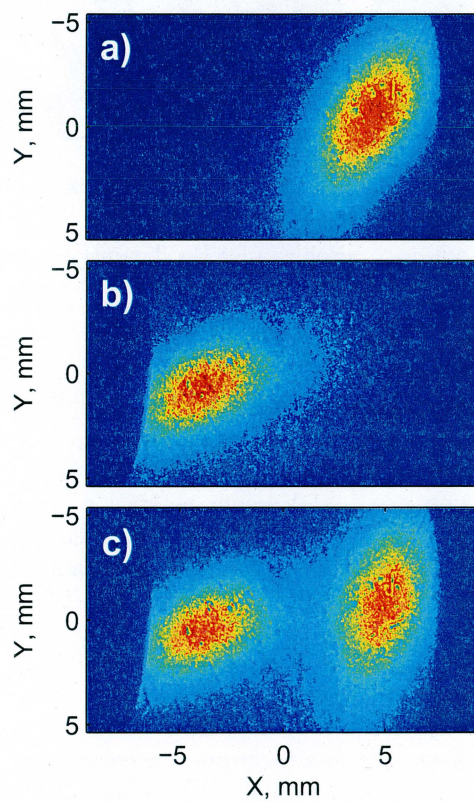


Figure 37: Demonstration of two independent harmonic beam generation. Images (a) and (b) are captured by blocking one of the two HHG pump beams. Image (c) suggests that two beams are generated independently.

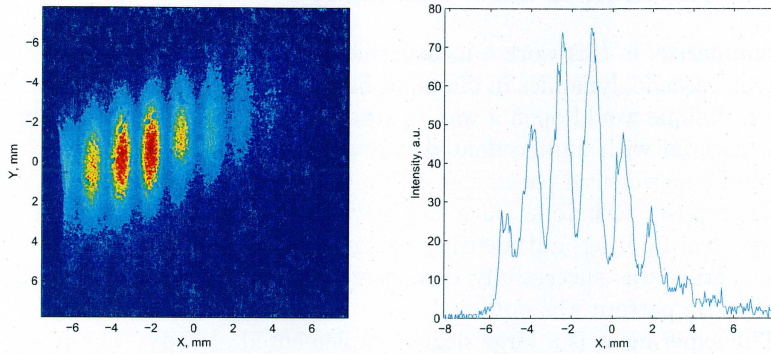


Figure 38: Two XUV beam interference pattern and lineout.

ble in order to have a large diffraction angle. Increasing the angle between the two XUV pump beams deteriorates the contrast of the interference fringes and the optimal value of the interference fringe period has to be found during the experiment. In the high contrast interference fringe pattern shown in Figure 38 six interference fringes are clearly visible. Although the XUV interference pattern was measured at a large distance from the focal plane of the Schwarzschild objective, the number of interference fringes is the same as in the plane where the sample will be placed. In case of the spot size $d_s = 20 \mu\text{m}$ on the sample, the period of interference fringes is then equal to $p = 3.3 \mu\text{m}$ and corresponds to an angle of diffraction of the probe beam equal to 14° . This angle of diffraction is large enough to separate a single diffraction maximum and to allow for easy detection. The angle between the two IR pump beams was $\theta_p = 0.089 \text{ mrad}$, which was measured from the fringe period $p_{ir} = 9 \text{ mm}$ of the infrared interference pattern. The relation between the fringe period and the angle between the two IR pump beams corresponds well to the estimations described in Section 2.3.3.

5 Conclusion and outlook

To summarize, in this work a measurement technique for the study of ultrafast electron cascade dynamics in diamond based on a transient grating is proposed. This technique would open a way to study high energy photon interaction with bulk material with unprecedented temporal resolution. An optical system design and experimental parameter estimation were done, indicating the viability of the proposed technique. As a step towards implementation of the experiment the spectral filtering and focusing using the same optical element with multi-layer coating was successfully demonstrated and high-contrast, high-intensity interference pattern was obtained.

The experiment is a large degree implemented already. The probe beam is set up and the three femtosecond pulses are overlapped in space and time. Also the detection part of the experiment is implemented.

5.1 Acknowledgements

First of all, I would like to thank Anne L'Huillier for giving me the opportunity to come to Lund. The idea of the transient gratings would have not been born without the fruitful discussions with Per Johnsson. I am grateful to Xinkui He for spending hours and hours explaining how to work with the high harmonic generation experimental setup. I am also grateful to Jörg, Markus and Rafal for numerous discussions and help in the lab. Marcus, thank you for the fluent Swedish translation of the abstract. It was a great pleasure to work in such a creative atmosphere.

A Schwarzschild objective parameters

The Schwarzschild objective is a two spherical mirror concentric system. For convenience it can be analyzed as a conventional refractive lens.

The ray matrices for the spherical mirrors:

$$M_{R_{1,2}} = \begin{pmatrix} 1 & 0 \\ -\frac{2}{R_{1,2}} & 1 \end{pmatrix} \quad (58)$$

The free-space propagation matrix between mirrors:

$$M_d = \begin{pmatrix} 1 & R_1 + R_2 \\ 0 & 1 \end{pmatrix} \quad (59)$$

The final ray transfer matrix for the objective is:

$$M_O = M_{R_2} M_d M_{R_1} = \begin{pmatrix} -2\frac{R_2}{R_1} - 1 & R_1 + R_2 \\ \frac{2}{R_1} + \frac{2}{R_2} & -2\frac{R_1}{R_2} - 1 \end{pmatrix} = \begin{pmatrix} A & B \\ C & D \end{pmatrix} \quad (60)$$

In our case, $R_1 = -33.9$ mm, $R_2 = 91.7$ mm. The parameters of the objective are listed in the Table 1.

Table 1: The Schwarzschild objective parameters	
Parameter	Description
$d_U = D(A - 1)/C - B = R_1$	Distance from front principal plane to the convex mirror
$d_{U'} = (1 - A)/C = R_2$	Distance from concave mirror to the rear principal plane
$d_{F'} = -A/C = \frac{R_2(R_1 + 2R_1)}{2(R_1 + R_2)}$	Distance from concave mirror to the rear focal plane
$f' = d_{F'} - d_{U'} = -1/C = \frac{R_1 R_2}{2(R_1 + R_2)}$	Rear focal length

An important feature is that both principal planes of the system coincide and are located at the center of curvature of both lenses. The Schwarzschild objective can be analyzed as a thin lens of focal length f' placed in the principal plane. A schematic of both mirrors is shown in Figure 39.

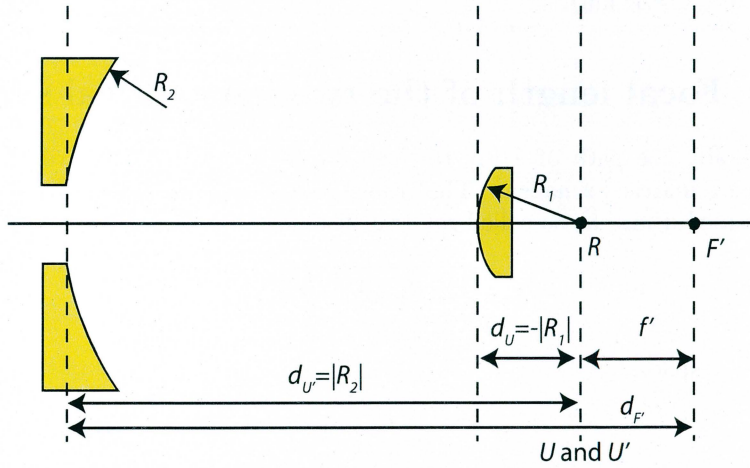


Figure 39: Schwarzschild objective principal points.

The Schwarzschild objective has the disadvantage that part of the incident beam is reflected back which significantly reduces its transmission. To avoid losing the photons, we send the beam off-axis. The disadvantage in this case is the increased aberration. Due to the off-axis geometry, after the objective the beam travels at an angle. The angle at the center of the clear aperture was measured to be $\alpha_0 = 8.6^\circ$. Minimum angle $\alpha_{min} = 6.2^\circ$, maximum angle $\alpha_{max} = 10.9^\circ$ as shown in Figure 40. From these angles the clear aperture can be calculated: $d_a = f' [\tan(\alpha_{max}) - \tan(\alpha_{min})] = 2.3$ mm. This means that the input beam diameter should not be larger than d_a or otherwise it will be clipped.

The numerical aperture is the difference of minimum and maximum acceptance angles: $NA = \sin(\alpha_{max} - \alpha_{min}) = 0.083$. From this we can estimate the

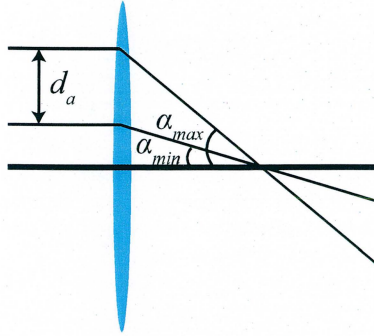


Figure 40: Minimum and maximum acceptance angles of the Schwarzschild objective.

resolution limited by the objective in off-axis configuration: $R = 1.22\lambda/\text{NA} = 0.56 \mu\text{m}$ (in case $\lambda = 38 \text{ nm}$).

B Focal length of the two-lens optical system

Generally the path of a ray through an element can be described using ray transfer matrix formalism. The transformation of beam angle and position is expressed using the so-called ray transfer matrix:

$$\begin{pmatrix} A & B \\ C & D \end{pmatrix} \quad (61)$$

Free space:

$$M_d = \begin{pmatrix} 1 & d \\ 0 & 1 \end{pmatrix} \quad (62)$$

lens:

$$M_l = \begin{pmatrix} 1 & 0 \\ -\frac{1}{f} & 1 \end{pmatrix} \quad (63)$$

To get the system matrix, the matrices of two lenses and free space propagation must be multiplied in the reverse order. The M_{l_2} is the ray transfer matrix of the first lens of focal length f_1 and M_{l_1} is the matrix of the second lens of focal length f_2 which is at distance d from the first lens.

$$M = M_{l_2} M_d M_{l_1} = \begin{pmatrix} 1 - \frac{d}{f_1} & d \\ \frac{d - f_1 - f_2}{f_1 f_2} & 1 - \frac{d}{f_2} \end{pmatrix} \quad (64)$$

Effective focal length:

$$f' = -\frac{1}{C} = \frac{f_1 f_2}{f_1 + f_2 - d} \quad (65)$$

Distance to the focus from the last lens:

$$d_{F'} = -\frac{A}{C} = f_2 - \frac{f_2^2}{f_1 + f_2 - d} \quad (66)$$

References

- [1] U. Keller, "Recent developments in compact ultrafast lasers," *Nature* **424**, 831–838 (2003).
- [2] J. Mauritsson, P. Johnsson, E. Mansten, M. Swoboda, T. Ruchon, A. L'Huillier, and K. J. Schafer, "Coherent Electron Scattering Captured by an Attosecond Quantum Stroboscope," *Physical Review Letters* **100**(7), 073003 (pages 4) (2008). URL <http://link.aps.org/abstract/PRL/v100/e073003>.
- [3] J. Isberg, J. Hammersberg, E. Johansson, T. Wikstrom, D. J. Twitchen, A. J. Whitehead, S. E. Coe, and G. A. Scarsbrook, "High Carrier Mobility in Single-Crystal Plasma-Deposited Diamond," *Science* **297**(5587), 1670–1672 (2002). <http://www.sciencemag.org/cgi/reprint/297/5587/1670.pdf>, URL <http://www.sciencemag.org/cgi/content/abstract/297/5587/1670>.
- [4] B. Ziaja, R. A. London, and J. Hajdu, "Unified model of secondary electron cascades in diamond," *Journal of Applied Physics* **97**(6), 064905 (pages 9) (2005). URL <http://link.aip.org/link/?JAP/97/064905/1>.
- [5] A. L'Huillier, D. Descamps, A. Johansson, J. Norin, J. Mauritsson, and C. G. Wahlström, "Applications of high-order harmonics," *The European Physical Journal D - Atomic, Molecular, Optical and Plasma Physics* **26**(1), 91–98 (2003). 10.1140/epjd/e2003-00072-2.
- [6] M. Bellini, C. Lyngå, A. Tozzi, M. B. Gaarde, T. W. Hänsch, A. L'Huillier, and C.-G. Wahlström, "Temporal Coherence of Ultrashort High-Order Harmonic Pulses," *Phys. Rev. Lett.* **81**(2), 297–300 (1998).
- [7] C. Rose-Petruck, R. Jimenez, T. Guo, A. Cavalleri, C. W. Siders, F. Raksi, J. A. Squier, B. C. Walker, K. R. Wilson, and C. P. J. Barty, "Picosecond-milliangstrom lattice dynamics measured by ultrafast X-ray diffraction. (cover story)," *Nature* **398**(6725), 310 – (1999).
- [8] P. A. Franken, A. E. Hill, C. W. Peters, and G. Weinreich, "Generation of Optical Harmonics," *Phys. Rev. Lett.* **7**(4), 118–119 (1961).

- [9] P. Agostini, F. Fabre, G. Mainfray, G. Petite, and N. K. Rahman, “Free-Free Transitions Following Six-Photon Ionization of Xenon Atoms,” *Phys. Rev. Lett.* **42**(17), 1127–1130 (1979).
- [10] M. Ferray, A. L’Huillier, X. F. Li, L. A. Lompre, G. Mainfray, and C. Manus, “Multiple-harmonic conversion of 1064 nm radiation in rare gases,” *Journal of Physics B: Atomic, Molecular and Optical Physics* **21**(3), L31–L35 (1988). URL <http://stacks.iop.org/0953-4075/21/L31>.
- [11] A. L’Huillier, M. Lewenstein, P. Salières, P. Balcou, M. Y. Ivanov, J. Larsson, and C. G. Wahlström, “High-order Harmonic-generation cutoff,” *Phys. Rev. A* **48**(5), R3433–R3436 (1993).
- [12] E. Seres, J. Seres, F. Krausz, and C. Spielmann, “Generation of Coherent Soft-X-Ray Radiation Extending Far Beyond the Titanium *L* Edge,” *Phys. Rev. Lett.* **92**(16), 163,002 (2004).
- [13] P. B. Corkum, “Plasma perspective on strong field multiphoton ionization,” *Phys. Rev. Lett.* **71**(13), 1994–1997 (1993).
- [14] K. J. Schafer and K. C. Kulander, “High Harmonic Generation from Ultrafast Pump Lasers,” *Phys. Rev. Lett.* **78**(4), 638–641 (1997).
- [15] M. Lewenstein, P. Balcou, M. Y. Ivanov, A. L’Huillier, and P. B. Corkum, “Theory of high-harmonic generation by low-frequency laser fields,” *Phys. Rev. A* **49**(3), 2117–2132 (1994).
- [16] K. C. Kulander and B. W. Shore, “Calculations of Multiple-Harmonic Conversion of 1064-nm Radiation in Xe,” *Phys. Rev. Lett.* **62**(5), 524–526 (1989).
- [17] T. Ruchon, C. P. Hauri, K. Varju, E. Mansten, M. Swoboda, R. Lopez-Martens, and A. L’Huillier, “Macroscopic effects in attosecond pulse generation,” *New Journal of Physics* **10**(2), 025,027 (10pp) (2008).
- [18] F. Lindner, G. G. Paulus, H. Walther, A. Baltuška, E. Goulielmakis, M. Lezius, and F. Krausz, “Gouy Phase Shift for Few-Cycle Laser Pulses,” *Phys. Rev. Lett.* **92**(11), 113,001 (2004).
- [19] A. Rundquist, I. Durfee, Charles G., Z. Chang, C. Herne, S. Backus, M. M. Murnane, and H. C. Kapteyn, “Phase-Matched Generation of Coherent Soft X-rays,” *Science* **280**(5368), 1412–1415 (1998). <http://www.sciencemag.org/cgi/reprint/280/5368/1412.pdf>, URL <http://www.sciencemag.org/cgi/content/abstract/280/5368/1412>.
- [20] C. G. Durfee, A. R. Rundquist, S. Backus, C. Herne, M. M. Murnane, and H. C. Kapteyn, “Phase Matching of High-Order Harmonics in Hollow Waveguides,” *Phys. Rev. Lett.* **83**(11), 2187–2190 (1999).

- [21] H. R. Lange, A. Chiron, J.-F. Ripoche, A. Mysyrowicz, P. Breger, and P. Agostini, “High-Order Harmonic Generation and Quasiphase Matching in Xenon Using Self-Guided Femtosecond Pulses,” *Phys. Rev. Lett.* **81**(8), 1611–1613 (1998).
- [22] M. Gabrysch, E. Marklund, J. Hajdu, D. J. Twitchen, J. Rudati, A. M. Lindenberg, C. Caleman, R. W. Falcone, T. Tschentscher, K. Moffat, P. H. Bucksbaum, J. Als-Nielsen, A. J. Nelson, D. P. Siddons, P. J. Emma, P. Krejčík, H. Schlarb, J. Arthur, S. Brennan, J. Hastings, and J. Isberg, “Formation of secondary electron cascades in single-crystalline plasma-deposited diamond upon exposure to femtosecond x-ray pulses,” *Journal of Applied Physics* **103**(6), 064909 (pages 6) (2008). URL <http://link.aip.org/link/?JAP/103/064909/1>.
- [23] R. A. Bartels, A. Paul, H. Green, H. C. Kapteyn, M. M. Murnane, S. Backus, I. P. Christov, Y. Liu, D. Attwood, and C. Jacobsen, “Generation of Spatially Coherent Light at Extreme Ultraviolet Wavelengths,” *Science* **297**(5580), 376–378 (2002). <http://www.sciencemag.org/cgi/reprint/297/5580/376.pdf>, URL <http://www.sciencemag.org/cgi/content/abstract/297/5580/376>.
- [24] D. G. Lee, J. J. Park, J. H. Sung, and C. H. Nam, “Wave-front phase measurements of high-order harmonic beams by use of point-diffraction interferometry,” *Opt. Lett.* **28**(6), 480–482 (2003). URL <http://ol.osa.org/abstract.cfm?URI=ol-28-6-480>.
- [25] R. Zerne, C. Altucci, M. Bellini, M. B. Gaarde, T. W. Hänsch, A. L’Huillier, C. Lyngå, and C.-G. Wahlström, “Phase-Locked High-Order Harmonic Sources,” *Phys. Rev. Lett.* **79**(6), 1006–1009 (1997).
- [26] D. Descamps, C. Lyngå, J. Norin, A. L’Huillier, C.-G. Wahlström, J.-F. Hergott, H. Merdji, P. Salières, M. Bellini, and T. W. Hänsch, “Extreme ultraviolet interferometry measurements with high-order harmonics,” *Opt. Lett.* **25**(2), 135–137 (2000). URL <http://ol.osa.org/abstract.cfm?URI=ol-25-2-135>.
- [27] M. Gabrysch, “Notes on LLC-Diamond Project,” .
- [28] X. He, M. Miranda, J. Schwenke, O. Guilbaud, T. Ruchon, E. Georgadiou, A. Persson, and A. L’Huillier. Unpublished.
- [29] “X-Ray atomic constant database,” URL <http://henke.lbl.gov>.
- [30] J. Schwenke, A. Mai, M. Miranda, X. He, G. Genoud, A. Mikkelsen, S.-G. Pettersson, A. Persson, and A. L’Huillier, “Single-shot holography using high-order harmonics,” *Journal of Modern Optics* **55**, 2723–2730 (2008).
- [31] D. Strickland and G. Mourou, “Compression of amplified chirped optical pulses,” *Optics Communications* **56**(3), 219 – 221 (1985).

- [32] S. Akturk, M. Kimmel, P. O'Shea, and R. Trebino, "Measuring spatial chirp in ultrashort pulses using single-shot Frequency-Resolved Optical Gating," *Opt. Express* **11**(1), 68–78 (2003). URL <http://www.opticsexpress.org/abstract.cfm?URI=oe-11-1-68>.
- [33] S. Akturk, M. Kimmel, P. O'Shea, and R. Trebino, "Measuring pulse-front tilt in ultrashort pulses using GRENOUILLE," *Opt. Express* **11**(5), 491–501 (2003). URL <http://www.opticsexpress.org/abstract.cfm?URI=oe-11-5-491>.
- [34] G. Pretzler, A. Kasper, and K. J. Witte, "Angular chirp and tilted light pulses in CPA lasers," *Applied Physics B: Lasers and Optics* **70**, 1–9 (2000).
- [35] R. W. Boyd, *Nonlinear Optics* (Nonlinear Optics, 2nd ed.. by R.W. Boyd. London: Academic Press, 2003 ISBN 9780121216825, 2003).